



# Clues of wildfire-induced geotechnical changes in volcanic soils affected by post-fire slope instabilities

Dario Peduto<sup>1</sup> · Luca Iervolino<sup>1</sup> · Giuseppe Esposito<sup>2</sup> · Vito Foresta<sup>1</sup> · Fabio Matano<sup>3</sup> · Rocco Masi<sup>4</sup>

Received: 20 April 2022 / Accepted: 18 September 2022  
© The Author(s) 2022

## Abstract

Wildfires can significantly affect mountain hillslopes through the combustion of trees and shrubs and changes in soil properties. The type and magnitude of the associated post-fire effects depend on several factors, including fire severity and soil physical–mechanical–hydraulic features that, coupled with climate and topographic conditions, may cause increased runoff, erosion, and slope instability as consequence of intense rainfall. The post-fire response of slopes is highly site-specific. Therefore, in situ surveys and laboratory tests are needed to quantify changes in key soil parameters. The present study documents the post-fire physical and hydromechanical properties of pyroclastic topsoil collected from three test sites that suffered wildfires and rainfall-induced post-fire events in 2019 and 2020 in the Sarno Mountains (Campania Region, southern Italy). The tested pyroclastic soils in burned conditions show (i) no significant changes in grain size distribution, soil organic matter, and specific gravity; (ii) a deterioration in shear strength in terms of decreased soil cohesion caused by the fire-induced weakening of root systems; and (iii) a decrease in hydraulic conductivity. Accordingly, it can be argued that the documented post-fire erosion responses were mainly caused by the reduced cohesion and hydraulic conductivity of the burned topsoil layer, as well as by the loss of vegetation cover and the deposition of fire residues. Although deserving further deepening, this study can represent the necessary background for understanding the initiation mechanism of post-fire erosion processes in the analyzed area and on several natural slopes under similar conditions.

**Keywords** Wildfire · Pyroclastic soils · Rooted soils · Shear strength · SWRCs · Soil erosion

---

✉ Luca Iervolino  
liervolino@unisa.it

Dario Peduto  
dpeduto@unisa.it

Giuseppe Esposito  
giuseppe.esposito@irpi.cnr.it

Vito Foresta  
vforesta@unisa.it

Fabio Matano  
fabio.matano@cnr.it

Rocco Masi  
rocco.masi@cimafoundation.org

<sup>1</sup> Department of Civil Engineering, University of Salerno, via Giovanni Paolo II, Fisciano (SA) 132 84084, Italy

<sup>2</sup> National Research Council, Research Institute for Geo-Hydrological Protection (CNR-IRPI), Perugia, Italy

<sup>3</sup> National Research Council, Institute of Marine Sciences (CNR-ISMAR), Naples, Italy

<sup>4</sup> CIMA Research Foundation, Savona, Italy

## Introduction

Wildfires leave a significant mark on the landscape through the combustion of trees and shrubs and changes in soil characteristics that may cause reduced infiltration of rainwater and consequently increased runoff and erosion compared to the unburned areas. Intensive erosive processes such as rill erosion, gully erosion, and channel erosion in burned areas have been documented worldwide (e.g., Benda et al. 2003; Rengers et al. 2016). The mobilization of sediments downstream and incorporation of additional material within the hydraulic flows along the drainage network may lead to sediment-laden and debris flows (Woods and Balfour 2008). These mass movements may occur as a consequence of intense rainfall within a few years after a fire and several times in the same burned basin (De Graff 2018; Staley et al. 2020). The relatively high flow velocities may increase the hazard and risk conditions for people living near the outlets of burned watersheds and thus exposed to the impact of flow processes.

Analyzing predisposing factors leading to post-fire soil erosion and debris flows involves different research fields, including geotechnical, geomorphological, and geological sciences. Generally, the fire-induced changes in geotechnical properties of soils are site-specific since the soil types may have different characteristics, mainly depending on geology, topography, and climate. In addition, wildfires can be characterized by variable intensities according to local conditions. Concerning the fire effects on soil geotechnical properties, there is much debate in the literature because information about modifications to physical or hydraulic characteristics is often discordant. For instance, previous studies have shown that grain size increases, decreases, or does not change depending on the soil type (Ulery and Graham 1993; Terefe et al. 2008; Stoof et al. 2010; Esposito et al. 2017). The effects of fire on the soil organic matter (SOM) content are also highly variable. These effects may range from the almost destruction of the SOM (Alauzis et al. 2004; García-Corona et al. 2004) to increases in the topsoil due to the deposition of dry leaves and partially burned plant materials (González-Pérez et al. 2004). Moreover, even no significant effects on SOM content were observed (Fernández et al. 1997; Badía and Martí 2003). The behavior of hydraulic conductivity is strongly variable as well. Literature studies report (i) decreases in post-fire hydraulic conductivity because of ash clogging/sealing soil pores and fire-induced soil hydrophobicity (Neary et al. 1999; Robichaud 2000; Shakesby and Doerr 2006); (ii) no change (Stoof et al. 2010), or (iii) even increases for severe fires, which can destroy the hydrophobic layer and form macropore flow pathways by burning the soil root systems (Lei et al. 2022). Besides this, very little information can be found on the fire effects on soil mechanical properties and their implication on debris flow occurrence. Moody et al. (2005) identified the critical shear stress as a reference parameter to analyze the inception of soil particle movement. It has been seen that this soil parameter depends on temperature; in particular, fire may burn some roots, contributing to a decrease in soil cohesion (Nakane et al. 1983) and causing soil friction angle variations (Tiwari et al. 2019) especially for more severe burns (Peduto et al. 2022). In addition, the mechanical properties of fire-affected hydrophobic soils have been tested, showing that soil shear strength decreases as soil hydrophobicity increases (Movasat and Tomac 2021). In a variable framework like this, research efforts should be focused on defining a clear scientific background able to support post-fire analyses adequately.

This paper aims at enhancing the existing knowledge about the effects of wildfires on geotechnical properties of soils originated from pyroclastic airfall deposits (i.e., andosols – WRB 2006) of the Campania region (southern Italy). The study sites occur within one of the most exposed areas to landslides in Italy since it was affected by multiple events in the past, including the disaster of 5–6 May 1998 (Cascini et al. 2011). In the

aftermath of such a disaster, much research was developed to analyze the geotechnical properties of pyroclastic layers and soil horizons involved in the slope failures in unburned conditions. Recent studies demonstrated that pyroclastic soils in this area are also susceptible to post-fire erosion processes (Esposito et al. 2013, 2017, 2019), which can supply hyper-concentrated and debris flows threatening the urban centers downstream. This study provides a preliminary characterization of the modifications to physical–mechanical and hydraulic properties of the topsoils affected by three wildfires in 2019 and 2020 (Fig. 1a), followed by rainfall-induced soil erosion processes a few weeks later. The research findings can be useful to improve the knowledge about mechanisms controlling post-fire erosion responses in similar areas and providing input data for implementing prediction models or planning in situ monitoring systems.

## The study area

### Geology, geomorphology, and past landslides

The study area is located in the Campania Region, southern Italy, along the southern slope of a carbonate massif formed by Mesozoic limestone and dolomite rocks (Di Nocera et al. 2011), and referred to as Sarno Mountains (Fig. 1). These latter reach a peak elevation of 1133 m above sea level and their morphology is characterized by steep slopes with average gradients of about 35°, decreasing to about 10° in the foot slope. The vertical continuity of the slopes is interrupted locally by vertical carbonate scarps extending laterally up to a few hundred meters. The scarps correspond to erosion profiles of thick carbonate beds, with heights ranging from 1–2 m to 10–15 m. Instead, the lateral continuity is interrupted by several stream valleys extending downslope from about the ridge crest, with lengths reaching up to 2 km and average depths around 30 m. Since the Late Quaternary, the massif was mantled by pyroclastic airfall deposits derived from multiple eruptions of the nearby Somma-Vesuvius volcanic complex (Rolandi et al. 1998).

The slope-mantling deposits consist of a thin layer of colluvial deposits made by reworked pyroclastic deposits locally mixed to calcareous debris, covering pyroclastic sequences made of alternating layers of ashes and pumices, locally interrupted by buried soil horizons. These deposits are classified as andosols (WRB 2006) and are characterized by different hydraulic and mechanical properties and negligible cohesion (Cascini and Sorbino 2002; Crosta and Dal Negro 2003; Bilotta et al. 2005; Picarelli and Vinale 2007; Damiano and Olivares 2010; De Vita et al. 2013). Accordingly, the shear strength of the volcanoclastic cover is controlled mainly by matric suction (Picarelli et al. 2020) and by plant roots in the surficial zone (Foresta et al. 2020). The well-developed

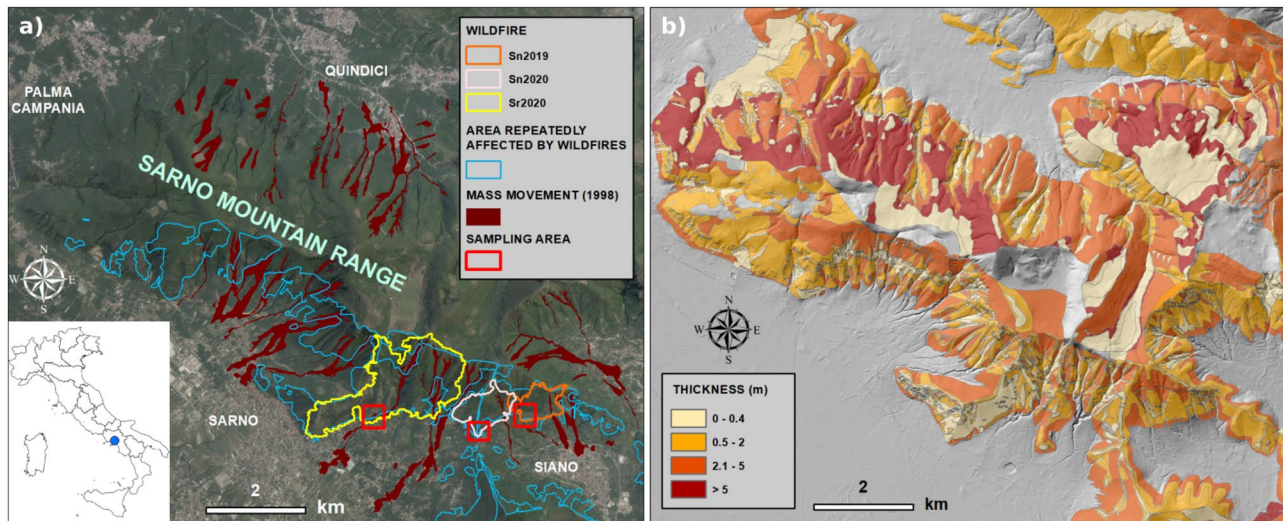


**Fig. 1** The study area of the Sarno Mountains with the indication of **a** the flowslides of 1998, the three burned areas in 2019 and 2020, the boundaries of past burned areas within the period 2000–2014, and sampling areas; **b** The pyroclastic cover thickness

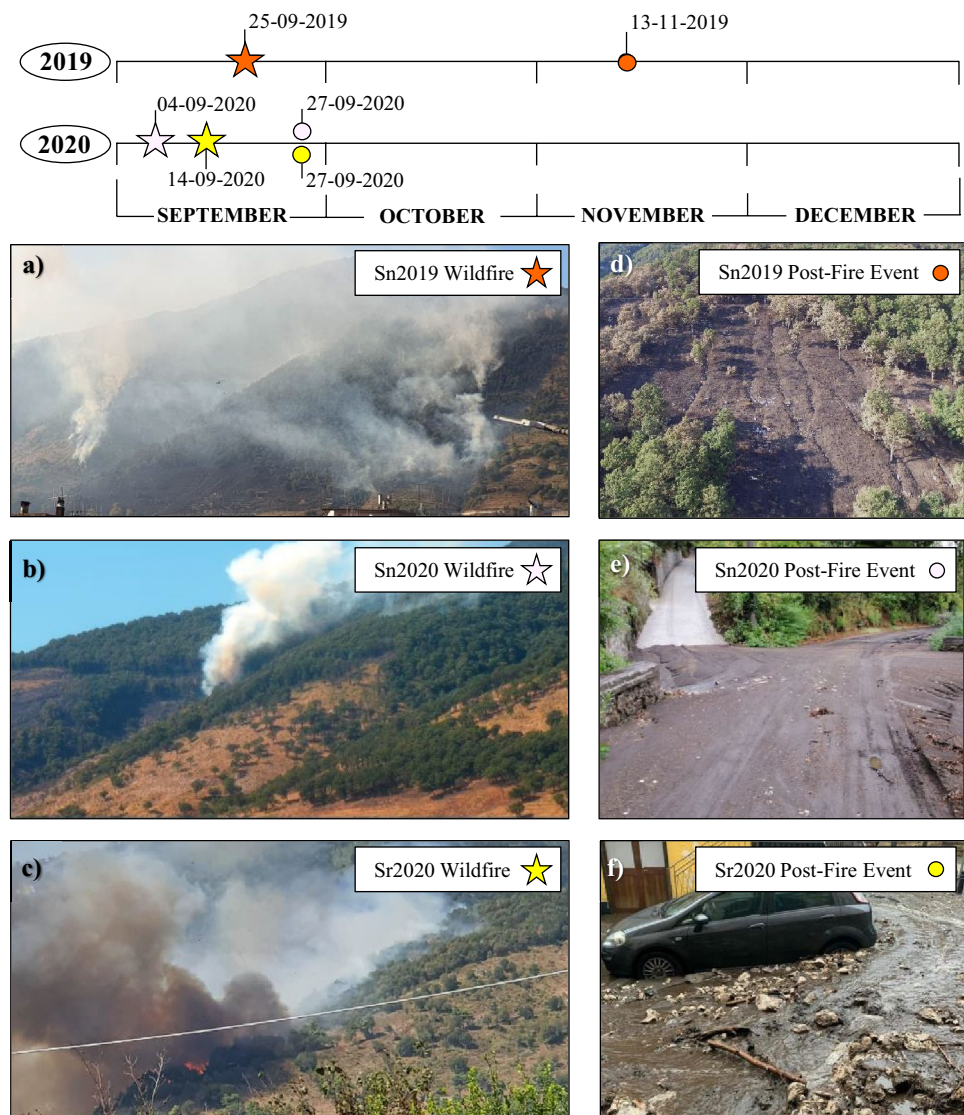
vegetation in the area, formed by oak, chestnut, and pine forests mixed with Mediterranean shrubs, represents a strong protection against surface erosion (Esposito et al. 2017). On the other side, this canopy cannot stabilize the entire volcanoclastic cover, as demonstrated by past landslides involving fully vegetated zones. The overall development of vegetation in the area is favored by a Mediterranean climate with hot, dry summers, and moderately cool, rainy winters, with average annual precipitations in the order of 1000–1200 mm.

The current volcanoclastic cover (Fig. 1b) is not continuous in the space since its thickness varies according to topography, as well as to the occurrence of mass movements and erosion processes. The thickness ranges from less than half a meter within the steepest areas (maximum slope angles up to 50°) to up to 5–7 m on gentle slopes (De Vita et al. 2013). The base of the massif is constituted by talus deposits, including reworked volcanoclastic material mixed with carbonate debris derived from slope instability processes. These latter include (i) rockfalls affecting the fractured carbonate scarps; (ii) shallow landslides involving the volcanoclastic cover; and (iii) post-fire surface erosion. All these processes were documented in the scientific literature developed after the geo-hydrological event on 5 and 6 May 1998. This event was characterized by hundreds of shallow landslides that occurred over the entire Sarno Mountain Range, involving the volcanoclastic deposits and uppermost strata of the carbonate bedrock (Fig. 1a). In many cases, initial debris slides (Cruden and Varnes 1996) evolved into debris avalanches (Hungr et al. 2001) before being channelized into the narrow gullies or channels in which the mobilized mass transformed into rapid and extremely rapid debris/hyperconcentrated flows

(Pearson et al. 1987; Cruden and Varnes 1996; Guadagno et al. 2005; Cascini et al. 2008). Overall, about 2,000,000 m<sup>3</sup> of pyroclastic sediments and carbonate rocks were displaced during the entire event (Cascini et al. 2008). The impact of flows on urban settlements caused 160 fatalities; 115 people were injured, 1210 became homeless, and severe damage to buildings and economic activities quantified in more than 30 million Euros (Brondi and Salvatori 2003).

Historical research documented a moderate frequency of events like this in the past centuries, both in the Sarno area and other parts of the region characterized by similar geological and geomorphological properties (Migale and Milone 1998; Calcaterra et al. 2000; Guadagno and Revellino 2005). Notwithstanding, no correlation was found with wildfires that, according to data from the National Forestry Corps, affect the Sarno Mountain Range with a relatively high annual frequency, especially during the summer season (<https://sit2.regione.campania.it/servizio/catasto-incendi>). On the other hand, Esposito et al. (2017, 2019) documented that erosion and flow processes are very likely in wildfire-affected areas due to intense rainstorms impacting the burned topsoils. Such rainstorms are often associated with frontal storms and isolated convective cells occurring mostly in the late summer-autumn period (De Luca et al. 2010), when most of the recorded post-fire erosion processes have occurred. It is worth noting that sediment-laden and debris flows characterizing post-fire responses (Fig. 2) have a relatively low magnitude with respect to flows similar to the ones occurred during the 1998 event. Despite this, the associated hazard and risk levels are very high if the potential impact on urban settlements is considered (e.g., Esposito et al. 2019 – Fig. 2).

**Fig. 2** Timeline showing the occurrence of wildfires and consequent post-fire responses. Photos of the wildfires (a, b, c) (credits: Croce Azzurra Siano volunteers) and post-fire events (d, e, f) are reported below



### Post-fire erosion responses

The three burned sites in the municipalities of Siano (Sn2019 and Sn2020) and Sarno (Sr2020) were also affected by post-fire erosion processes and consequent floodings in the weeks following the fire events (Fig. 2). Rainstorms characterized by sub-hourly durations (i.e., 30 and 50 min) triggered erosion responses in November 2019 and September 2020 with peak 10-min rainfall intensities of 50 and 102 mm/h, respectively, according to the data recorded by a rain gauge of the Civil Protection located about 3000 m from the burned sites. The average storm intensities resulted in 25.2 and 51 mm/h. In the burned watersheds, both hyper-concentrated and debris flows took place, overwhelming the urban settlements downstream and damaging some buildings along with parked vehicles (Fig. 2). Some images acquired using a UAV in the aftermath of the Sn2019 post-fire event highlighted several rill networks developed along the burned

slopes, demonstrating that part of the sediment was mobilized by concentrated surface runoff during the rainstorm before being deposited along the underlying road.

### Materials and methods

Figure 3 shows the procedure followed to investigate changes in soil geotechnical properties because of fires characterized by different burn severity. It consists of two main steps: (i) in situ assessment of the fire burn severity and sampling; (ii) geotechnical laboratory tests on undisturbed soil samples.

Soil sampling was essential to perform geotechnical laboratory tests on undisturbed samples. It was conducted in 0–5 cm depth to limit the analysis to the shallow fire-affected topsoil layer. Undisturbed soil samples were collected in the three test sites on different dates to appreciate any changes in geotechnical properties of post-fire soils. To prevent from

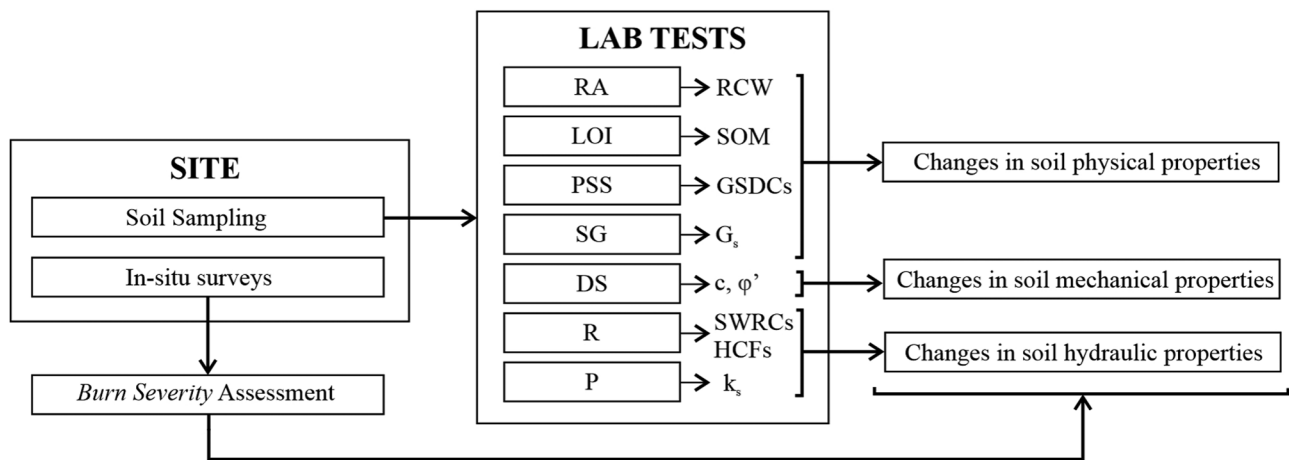


**Fig. 3** Workflow used to analyze the fire effects on the topsoil physical, mechanical, and hydraulic properties (RA, root analysis; LOI, loss on ignition; PSS, particle-size by sieving; SG, specific gravity; DS, direct shear; R, retention; P, permeability)

changes of soil properties due to spatial variability, single and multiple sampling locations were randomly selected within accessible homogeneous areas (i.e., plots), which were qualitatively derived from the field investigations carried out. Each plot was characterized by homogeneous basic features (e.g., vegetation type, root system condition, etc.). In particular, with reference to the burned areas, we classified each plot according to the specific level of burn severity recorded. In this regard, in situ burn severity was assessed according to the procedure proposed by Parsons et al. (2010), through field surveys conducted for each burned site seven days after the fire events. The primary objective was to identify fire damage on the three sampling sites and document changes in the ecosystem and topsoil conditions. The mean characteristics considered to assess the burn severity were ground cover, ash color and depth, soil structure, and roots condition. Ground cover refers to effective organic cover that mitigates runoff and erosion and includes litter, duff, and woody debris. Ash color and depth include information on the color and depth of ash (on the order of cm). Soil structure refers to the adhesive contribution of the SOM, which binds soil particles into stable aggregates against detachment. Roots condition indicates the degree of change in roots because of fire. To estimate changes from pre-fire conditions, burned and unburned areas (Control Sn2019, Control Sn2020) characterized by similar soil and vegetation were compared. For each burned site, soil burn severity was assessed in pits close to the sampling points considered for the geotechnical analyses. The results of the burn severity assessment were summarized into five classes (Low, Moderate-Low, Moderate, Moderate-High, High).

The laboratory testing program included (i) Roots Analysis (RA) (no. 37); (ii) Loss-on-Ignition (LOI) tests (no. 29); (iii) Particle-size by dry-sieving (PSS) tests (no. 45); (iv)

Pycnometer Method (PM) tests (no. 45); (v) Direct Shear (DS) tests (no. 32); (vi) Retention (R) tests (no. 4); and (vii) Permeability (P) tests (no. 2).

The RA aimed to quantify the Root Content by Weight (RCW) in the samples used for the DS tests. For this purpose, the procedure shown by Schuurman and Goedewaagen (1971) was adopted. Precisely, after the DS tests, the samples were washed to extract the roots, removing all soil particles and impurities around them. Afterward, the roots were tipped out onto a fine gauze, moisture was pressed out, and then they were transferred to a small paper bag with tweezers. Finally, the roots were dried at 75 °C, preventing them from pulverizing. After drying for about 48 h, the bags of roots were placed in a desiccator to cool. The roots were then weighed. Starting from the RCW for each of the DS tested soil samples, the dimensionless parameter known as Root Volume Density (RVD) was then derived (Zhu and Zhang 2016) as the ratio between the total volume filled with the roots ( $V_r$ ) and the total volume ( $V_{tot}$ ) of the tested soil sample at the initial stage of the DS test, equal to the initial nominal volume of the employed cross-sectional square-shaped samples ( $L = 60$  mm and  $H = 20$  mm):

$$RVD(\%) = \frac{V_r}{V_{tot}} \times 100 \tag{1}$$

$V_r$  values were calculated as the ratio between the available RCW values (g) and the unit weight of the roots ( $\gamma_r = 0.63$  g/cm<sup>3</sup>), assumed in this work as that reported by Foresta et al. (2020), who investigated more in details the physical and mechanical properties of soil grass roots under similar conditions.

LOI tests are widely used for measuring the SOM content. SOM is oxidized at 500–550 °C to carbon dioxide and

ash. The weight loss during this reaction is easily measured by weighing the samples before and after heating and is closely correlated to the organic matter of the sediment (Dean 1974; Bengtsson and Enell 1986). All LOI analyses were carried out in a muffle furnace. For this study, the procedure described in the ASTM D7348-08 (2011) was followed. LOI temperatures close to those proposed by Dean (1974) and Bengtsson and Enell (1986) (i.e., 550 °C for two hours) were adopted. LOI values were calculated using the following equation:

$$\text{LOI} [\%] = \left( \frac{W_{105} - W_{550}}{W_{105}} \right) * 100 \quad (2)$$

wherein  $W_{105}$  represents the dry weight of the sample before combustion and  $W_{550}$  the dry weight after heating to 550 °C for two hours (both in g).

PSS tests were performed to determine the grain size distribution curves (GSDCs) following the procedure illustrated in the standard reference ASTM D422-63 (2007).

The specific gravity ( $G_s$ ) of each soil sample was computed by following the standard pycnometer method (PM) ASTM D 854 (2014).

Saturated DS tests were conducted on undisturbed soil specimens measuring 60 mm × 60 mm × 20 mm. The ASTM D3080 (2011) standard procedure was followed. To reflect the low-stress levels characterizing the in situ conditions of the analyzed topsoil layer, the adopted vertical stresses ( $\sigma'_{vc}$ ) were fixed to 9, 15, 20, and 29 kPa. DS tests were carried out in a shear testing device, applying a lateral displacement velocity of 0.0124 mm/min derived from information on the consolidation time of the tested specimens.

Transient fields of water content and pressure head in variably saturated soil slopes are determined by Richards' equation (Richards 1931):

$$\nabla \cdot k(h) \nabla H = \frac{\partial \theta_w(h)}{\partial t} \quad (3)$$

where  $h$  is the pressure head or suction head;  $H$  is the total head (i.e., the sum of suction head and elevation);  $k(h)$  is the hydraulic conductivity function (HCF);  $\theta_w(h)$  is the pressure-head dependent volumetric water content. The relationship between pressure head and water content is known as soil water retention curve (SWRC). In order to solve Eq. (3) for fields of suction head and water content, two characteristic functions, SWRC and HCF, must be defined and known.

The scientific literature highlights that the soil hydraulic behaviour is characterized by hysteresis (e.g., Mualem 1976a; Wheeler et al. 2003; Tami et al. 2004; Li 2005; Tarantino 2009; Yang et al. 2012; Pirone et al. 2014; Chen et al. 2019; Rianna et al. 2019; Comegna et al. 2021). The hysteresis can affect the effective in situ soil hydrological response at the beginning of critical rainfall events, with permeability and

volumetric water content at a given suction on a wetting path distinguished by a lower value than those on the corresponding drying path. The effective field hydrological paths generally develop along different scanning curves, which depend on the state of the reversal point in the process of successive wetting and drying.

The soil hysteretic nature has been known for a long time. However, in many engineering applications, the soil is assumed to be nonhysteretic since the measurement of a complete set of hysteretic SWRCs is extremely time consuming and costly (Lu and Likos 2004; Tsai 2010).

In this work, Soil Water Retention Curves (SWRCs) were derived by continuously drying undisturbed and initially saturated soil specimens (measuring 2461 mm<sup>2</sup> × 20 mm) according to a specific hydraulic path known as “main drying curve.” For the purpose of the main drying SWRCs determination, a suction-controlled oedometer, described in detail by Aversa and Nicotera (2002), was adopted. This apparatus can control the stress state variables identified by the net vertical stress ( $\sigma_v - u_a$ ) and the matric suction  $\psi = (u_a - u_w)$ , where  $\sigma_v$  is the total stress,  $u_a$  the pore-air pressure, and  $u_w$  the pore-water pressure (Fredlund and Rahardjo 1993). Matric suction can be explained as pore-water pressure with a negative value with respect to the pore-air pressure. The changes in the water content within soil pores result in changes in matric suction. Hence, the water flow within the unsaturated soil is affected by the less water-filled spaces among solid particles. As a result, the permeability of the unsaturated soil varies with the changes in matric suction (Fredlund and Rahardjo 1993). The variation range of the applicable matric suction depends on the air-entry value (AEV) of the adopted porous plate. A 100-kPa porous plate was used in this work.

There are several models for the SWRC and HCF; here, the widely used van Genuchten's model for the SWRC (see Eq. (4)) and van Genuchten–Mualem's model (see Eq. (5)) for the HCF (Mualem 1976b; van Genuchten 1980) with respect to matric suction  $\psi$  were adopted:

$$\frac{\theta_w - \theta_r}{\theta_s - \theta_r} = \left[ \frac{1}{1 + (\alpha\psi)^n} \right]^m \quad (4)$$

$$K = K_s \frac{\{1 - (\alpha\psi)^{n-1} [1 + (\alpha\psi)^n]^{-m}\}^2}{[1 + (\alpha\psi)^n]^{\frac{m}{2}}} \quad (5)$$

wherein  $\theta_w$  is the volumetric water content (i.e., the fraction of the total volume of soil occupied by the water contained in the soil);  $\theta_s$  is the saturated volumetric water content;  $\theta_r$  is the residual volumetric water content;  $K_s$  is the saturated hydraulic conductivity; and  $\alpha$ ,  $n$ ,  $m$  represents curve fitting parameters. Van Genuchten's model fitting parameters ( $\alpha$ ,

m, and n) control part of the S-shape curve. The effect of  $\alpha$  is closely related to the reciprocal of the AEV of a soil. The AEV is a critical value of suction, at which the largest pores in the soil matrix start losing water. Coarse-grained soils have a low AEV and a high  $\alpha$  value, whereas fine-textured soils have a lower  $\alpha$ . The n parameter gives information about the soil pore-size distribution. In particular, the n parameter controls the slope of the curve and reflects the width of the voids size distribution. It is known that a unit increase in suction at or near the steepest part of the curve causes more water to be extracted from coarse-textured soils (high n) than from fine-textured soils (low n), but not at other places of the SWRC. Finally, the m parameter refers to the asymmetry of the model and is correlated to the n parameter.

Permeability (P) tests were performed on undisturbed samples to determine the saturated hydraulic conductivity ( $K_s$ ) of the burned (B1) and revegetated (B2) samples. Constant head tests were carried out, and Darcy's law was applied according to the standard method (ISO 2004):

$$K_s = \frac{qL}{A \Delta h t} \quad (6)$$

where q is the infiltration water amount within the time interval t, L is the height of the sample, A is the cross-sectional area of the sample, and  $\Delta h$  is the pressure head difference.

## Results

Field surveys led to burn severity assessment of the three sites under study (Fig. 1a), where undisturbed soil samples were collected. The physical and hydromechanical properties of unburned (UB), burned (B1), and revegetated (B2) soil samples were investigated.

### Field investigations

The three sampled areas (Fig. 1a) are characterized by a complex stratigraphy of the pyroclastic deposits due to the interplay among several eruptive phases from the Somma-Vesuvius volcanic complex and the development of erosive and pedogenic processes over the slopes. The total thickness of ash-fall deposits fallen on the Sarno and Siano sites due to the Sarno (17 ka), Ottaviano (8 ka), Avellino (3.5 ka), Pompei (AD 79), Pollena (AD 472), and Montagna di Somma (AD 1631) eruptions ranges from 4 to 7 m (De Vita et al. 2006). Complete pyroclastic series can be found only in conservative morphological areas, usually characterized by slope angles lower than about 28°. Between 28 and 50 slope angles, the erosive



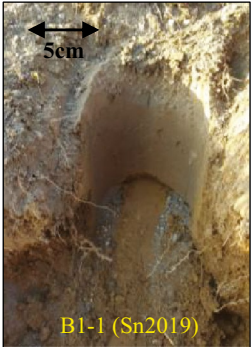


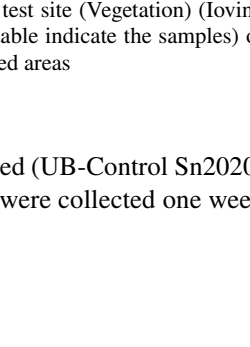

processes usually reduce the remaining soil thickness and over 50° only carbonate bedrock outcrops (De Vita and Napi 2011).

The pyroclastic stratigraphy (Cascini et al. 2000; De Vita and Napi 2011) shows a thin upper layer of highly organic soil, followed by a horizon formed by weathered and pedogenised fine and coarse pumiceous ashes in a silty colluvial matrix up to 1 m thick. They usually lie on the AD 472 eruption layer, formed by 0.3 to 1.2 m thick well to poorly graded pumice from coarse ash to lapilli in grain size, that had buried strongly weathered fine ash, sand with silt deposits (1- to 2-m-thick paleosoil). Then, we may have a further pumiceous buried horizon, attributed to the Avellino eruption (3.6 ky), resting on older strongly weathered fine ash and silty sand deposits, representing a buried paleosoil. Older pumice and paleosoils horizons can also be found between about 3 to 7 m of depth, and finally, the bedrock consists of fractured carbonate rocks.

The study sites are distinguished by different vegetation types (Fig. 4). In particular, the Sn2019 burned site is dominated by the presence of shrubs on terraced fields that are no longer cultivated (Tree Height: 0.5 m), whereas the corresponding unburned control site consists in degraded oak forests with a predominance of turkey oaks and/or downy oaks (tree height, 2.5 m). The Sr2020 site is characterized by herbaceous vegetation with occurrence of chestnut coppices (tree height, 1.5 m). Finally, holm oak forests (tree height, 7.5 m) dominate over the Sn2020 burned site, as well as the related unburned control site. Overall, plant roots condition was found different between unburned (UB) and fire-affected (B1, B2) sample classes. In particular, under unburned (UB) condition, the roots were characterized by a color tending toward brown, as well as non-negligible stiffness and elasticity. In contrast, the B2 samples, and to a greater extent the B1 samples, exhibit predominantly black roots, due to the fire-induced combustion. Such fire-affected roots were characterized by being drier and having lower stiffness and elasticity than those of the UB control sites. In addition, unlike the UB samples, which exhibit a root system characterized by several sub-systems (primary, secondary and tertiary roots), for the burned samples, we found only the presence of the primary roots probably because the sub-systems had been weakened by the fires and eventually lost.

Given the difficulty to assess and describe the root systems under pre-fire condition, in this paper we assume that the pre-fire root systems conditions for the Sn2019 and Sn2020 sites can be equated with those of the corresponding unburned control sites.

Undisturbed soil samples (Fig. 4) were collected in the Sn2019 burned area one week (B1-Sn2019) and five months after the fire event (B2-Sn2019); in addition, it was possible to collect unburned samples (UB-Control Sn2019) located

| Test Site         | Sample | Coordinates [m] |         | Burn Severity [-] | Slope [°] | Soil depth [m] | Vegetation [-]  |    |
|-------------------|--------|-----------------|---------|-------------------|-----------|----------------|---|---|
|                   |        | E               | N       |                   |           |                |   |   |
| Control<br>Sn2019 | UB-1   | 472856          | 4517894 |                   | 19.4      | 0.5-2          | degraded oak forests with a predominance of turkey oaks and/or downy oaks |    |
|                   | UB-2   | 472874          | 4517888 |                   | 19.5      | 0.5-2          |   |   |
|                   | UB-3   | 472868          | 4517904 | -                 | 21.7      | 0.5-2          |   |   |
|                   | UB-4   | 472855          | 4517912 |                   | 19.9      | 0.5-2          |   |   |
|                   | UB-5   | 472860          | 4517927 |                   | 18.3      | 0.5-2          |   |   |
| Control<br>Sn2020 | UB-6*  | 472014          | 4517618 |                   | 10.7      | 0-0.5          | holm oak forests  |    |
|                   | UB-7   | 472011          | 4517607 |                   | 10.6      | 0.5-2          |   |   |
|                   | UB-8   | 472025          | 4517617 |                   | 10.4      | 0-0.5          |   |   |
|                   | UB-9   | 472024          | 4517600 | -                 | 10.6      | 0-0.5          |   |   |
|                   | UB-10  | 472029          | 4517592 |                   | 10.7      | 0-0.5          |   |   |
|                   | UB-11  | 472044          | 4517595 |                   | 14.2      | 0-0.5          |   |   |
| Sn2019            | B1-1*  | 473196          | 4517942 | Mod-Low           | 20.0      | 0.5-2          | Terraced Fields which are no longer cultivated                            |   |
|                   | B1-2   | 473182          | 4517968 | Low               | 33.7      | 0.5-2          |   |   |
|                   | B1-3   | 473147          | 4518009 | Low               | 27.5      | 0.5-2          |   |   |
|                   | B1-4   | 473218          | 4518037 | Mod-Low           | 30.3      | 0.5-2          |   |   |
|                   | B1-5   | 473151          | 4518067 | Low               | 36.3      | 0.5-2          |   |   |
|                   | B2-1   | 473196          | 4517945 |                   | 20.0      | 0.5-2          | Terraced Fields which are no longer cultivated                            |  |
|                   | B2-2   | 473183          | 4517967 |                   | 28.5      | 0.5-2          |   |   |
|                   | B2-3   | 473145          | 4518011 | -                 | 26.7      | 0.5-2          |   |   |
|                   | B2-4   | 473222          | 4518042 |                   | 30.5      | 0.5-2          |   |   |
|                   | B2-5   | 473149          | 4518069 |                   | 36.3      | 0.5-2          |   |   |
| Sr2020            | B1-1*  | 469772          | 4517975 | Mod-High          | 9.2       | >5             | areas with herbaceous vegetation with occurrence of chestnut coppices     |  |
|                   | B1-2   | 469791          | 4517955 | High              | 10.2      | >5             |   |   |
|                   | B1-3   | 469784          | 4517939 | High              | 11.8      | >5             |   |   |
|                   | B1-4   | 469837          | 4517954 | Mod-High          | 8.7       | >5             |   |   |
|                   | B1-5   | 469823          | 4517934 | Mod-High          | 10.0      | >5             |   |   |
|                   | B1-6   | 469848          | 4517921 | Mod-High          | 9.6       | >5             |   |   |
|                   | B1-7   | 469865          | 4517912 | High              | 9.2       | >5             |   |   |
|                   | B1-8   | 469824          | 4517904 | High              | 9.8       | >5             |   |   |
|                   | B1-9   | 469837          | 4517893 | High              | 9.8       | >5             |   |   |
|                   | B2-1   | 469770          | 4517971 |                   | 10.7      | >5             | areas with herbaceous vegetation with occurrence of chestnut coppices     |   |
| B2-2              | 469793 | 4517957         |         | 10.2              | >5        |                |   |   |
| B2-3              | 469780 | 4517941         |         | 11.8              | >5        |                |   |   |
| B2-4              | 469835 | 4517960         |         | 10.4              | >5        |                |   |   |
| B2-5              | 469830 | 4517931         |         | 9.9               | >5        |                |   |   |
| B2-6              | 469852 | 4517925         | -       | 9.6               | >5        |                |   |   |
| B2-7              | 469867 | 4517914         |         | 9.2               | >5        |                |   |   |
| B2-8              | 469834 | 4517905         |         | 9.8               | >5        |                |   |   |
| B2-9              | 469839 | 4517895         |         | 9.9               | >5        |                |   |   |
| B2-10             | 469842 | 4517899         |         | 9.8               | >5        |                |   |   |
| Sn2020            | B1-1*  | 471972          | 4517629 | High              | 19.6      | 0.5-2          | holm oak forests  |  |
|                   | B1-2   | 471981          | 4517652 | High              | 22.2      | 0.5-2          |   |   |
|                   | B1-3   | 471981          | 4517674 | High              | 22.0      | 0.5-2          |   |   |
|                   | B1-4   | 471989          | 4517663 | Mod-High          | 21.0      | 0.5-2          |   |   |
|                   | B1-5   | 471990          | 4517635 | Mod-High          | 19.4      | 0.5-2          |   |   |

**Fig. 4** Soil samples information sheet. The table, distinguishing the different sample classes (i.e., UB: unburned samples, B1: burned samples collected soon after the fires, B2: burned samples collected 5 months and 8 months after the Sn2019 and Sr2020 wildfires, respectively) for each test site, shows (i) the coordinates of the sampling point expressed in the UTM 33 N–WGS84 system; (ii) the burn severity assessment (from low to high) of each burned sampling point

according to Parson’s procedure (Parsons et al. 2010); (iii) the slope of each sampling point obtained with a 5 × 5 m DTM (Digital Terrain Model); (iv) the depth of the pyroclastic cover at each sampling point; (v) the type of vegetation in each test site (Vegetation) (Iovino 2007); and (vi) photos (asterisks in the table indicate the samples) of soil collected in both unburned and burned areas

in the proximity of the burned area. The Sr2020 fire area only allowed the collection of burned samples one week (B1-Sr2020) and eight months after the fire (B2-Sr2020).

As for the Sn2020 fire site, unburned (UB-Control Sn2020) and burned (B1-Sn2020) samples were collected one week after the fire.



**Table 1** Soil burn severity assessment in each burned test site according to Parsons' procedure (Parsons et al. 2010)

| Test site | Ground cover* | Ash color   | Ash depth | Soil structure | Roots   | Soil burn severity |
|-----------|---------------|-------------|-----------|----------------|---------|--------------------|
| Sn2019    | 75%           | Brown/black | 2 cm      | No change      | Charred | Low/Mod-Low        |
| Sr2020    | 25%           | Black/grey  | 5 cm      | Changed        | Charred | Mod-High/High      |
| Sn2020    | 25%           | Grey/white  | 6 cm      | Changed        | Charred | Mod-High/High      |

\*Ground cover refers to effective unburned organic cover (e.g., litter, duff, ground fuels, vegetation needles, and leaves)

The investigated burned sites exhibited different soil burn severity (Fig. 4 and Table 1). Indeed, the Sn2019 sampling site was characterized by low/moderate-low burn severity, whereas both Sr2020 and Sn2020 sites showed a moderate-high/high burn severity. As for the Sn2019 site, surface organic layers were not completely consumed (75% of the pre-fire ground cover and surface organic matter were not consumed). The ground color appeared brown/black (lightly charred), the understory vegetation was green, and scorched needles or leaves (mostly intact) were found within the topsoil layer. Soil structure was not changed from its unburned condition (Control Sn2019), and roots were partially scorched. Regarding the Sr2020 site, 25% of the pre-fire ground cover and surface organic matter (litter, duff, and fine roots) was not consumed. The dominant color of the site was black. Ash and charcoal layers (up to 5 cm) were found. Soil structure decreased because of the consumption of organic matter and the deposition of fire residues. The soil appeared loose- and single-grained. Most roots were found to be consumed or charred. Concerning the Sn2020 sampling site, 25% of the pre-fire ground cover and surface organic matter (litter, duff, and fine roots) was not destroyed. The prevailing color of the site was grey. A layer of grey ash (up to 6 cm) was found along the burned slope. Soil structure was less stable than the unburned condition (Control Sn2020) because of the consumption of organic matter and ash deposition. The soil appeared loose, and most roots were found to be consumed or charred.

## Soil physical properties

Figure 5 shows the main physical properties of the analyzed soil samples for the unburned (Control Sn2019 and Control Sn2020) and burned (Sn2019, Sr2020, Sn2020) test sites.

Overall, the UB and B2 samples are characterized on average by higher RCW than the corresponding B1 samples, showing significant standard deviations due to the marked spatial variability of roots content within the tested topsoil layer (Fig. 5a). Specifically, as for the Sn2019 fire, a shift from an average RCW of  $0.20 \text{ g} \pm 0.19 \text{ g}$  (UB) to values lower than  $0.01 \text{ g}$  (B1) and then to  $0.10 \text{ g} \pm 0.10 \text{ g}$  (B2) is observed. Samples burned from the Sr2020 fire (B1) record an average RCW of  $0.02 \text{ g} \pm 0.02 \text{ g}$ , whereas those collected

eight months after the fire (B2) of  $0.23 \text{ g} \pm 0.18 \text{ g}$ . The Sn2020 B1 samples exhibit an average RCW of less than  $0.01 \text{ g}$ , whereas the corresponding UB of  $0.15 \text{ g} \pm 0.10 \text{ g}$ .

SOM content expressed by LOI is highly site-specific because it mainly depends on the vegetation and soil type. Moreover, it can also depend on the degree of combustion reached during the fire and thus on soil burn severity. As for the sites under study, Fig. 5b shows that the combined effects of the abovementioned factors do not appear to have significantly affected SOM values. Indeed, on average, the UB and B2 samples exhibit a negligible difference in LOI values compared to the B1 samples. Focusing on the Sr2020 site, the average LOI of the burned samples (B1,  $11.1\% \pm 1.9\%$ ) is similar to the revegetated ones (B2,  $11.8\% \pm 3.2\%$ ). As for the Sn2020 site, the UB and B1 samples show similar LOI values of  $12.2\% \pm 5.0\%$  and  $10.35\% \pm 4.4\%$ , respectively.

The specific gravity of the soil ( $G_s$ ) is related to LOI. Therefore, it also revealed its site-specificity, depending on the amount and type of organic matter within the soil samples. The results of the Sn2019 site show changes in  $G_s$  because of fire, with higher values for the UB and B2 samples than for the B1 samples (Fig. 5c). In contrast, the Sr2020 and Sn2020 sites exhibit no significant changes in  $G_s$  among the tested sample classes. Particularly, the Sn2019 soil ranges from  $G_s$  values of  $2.55 \pm 0.05$  for the UB samples to values of  $2.42 \pm 0.08$  (B1) and  $2.58 \pm 0.12$  (B2). The burned samples from the Sr2020 fire (B1) are characterized by  $G_s$  values of  $2.51 \pm 0.04$ , whereas the revegetated ones (B2) of  $2.47 \pm 0.05$ . The burned samples from Sn2020 (B1) exhibit  $G_s$  values of  $2.54 \pm 0.05$ , whereas the corresponding UB show values of  $2.57 \pm 0.06$ .

Overall, according to the Unified Soil Classification System (USCS), the Grain Size Distribution (GSD) of all analyzed samples ranges from silt in sand (MS, gravel = 10%, sand = 57%, silt = 33%) to well-graded gravel (GW, gravel = 53%, sand = 44%, silt = 3%). By considering each site (Fig. 5d), the GSD of the Sn2019 soil does not change on average for the three sample classes (UB, gravel = 20%, sand = 65%, silt = 15%; B1, gravel = 22%, sand = 58%, silt = 20%; B2, gravel = 14%, sand = 65%, silt = 22%), resulting as silt in sand (MS). Similar behaviors are recorded for the Sr2020 and Sn2020 sites, where the GSD of the samples does not significantly change on

| Test Site      | Sample | Roots [g] | LOI [%] | G <sub>s</sub> [-] | Silt+Clay [%] | Sand [%] | Gravel [%] |
|----------------|--------|-----------|---------|--------------------|---------------|----------|------------|
| Control Sn2019 | UB-1   | NA        | NA      | 2.48               | 16.9          | 61.1     | 22.0       |
|                | UB-2   | NA        | NA      | 2.57               | 20.4          | 64.1     | 15.5       |
|                | UB-3   | NA        | NA      | 2.56               | 22.4          | 57.0     | 20.6       |
|                | UB-4   | 0.06      | NA      | 2.60               | 3.6           | 76.7     | 19.7       |
|                | UB-5   | 0.33      | NA      | 2.53               | 14.1          | 62.7     | 23.2       |
| Control Sn2020 | UB-6   | <0.01     | 8.14    | 2.62               | 19.5          | 67.9     | 12.7       |
|                | UB-7   | 0.31      | 9.16    | 2.54               | 20.5          | 55.3     | 24.2       |
|                | UB-8   | 0.16      | 19.35   | 2.49               | 18.7          | 65.4     | 15.9       |
|                | UB-9   | 0.11      | 15.44   | 2.49               | 19.4          | 66.8     | 13.8       |
|                | UB-10  | 0.14      | 8.84    | 2.55               | 19.4          | 64.0     | 16.6       |
|                | UB-11  | 0.16      | NA      | 2.55               | 20.5          | 58.5     | 21.0       |
| Sn2019         | B1-1   | NA        | NA      | 2.53               | 20.6          | 50.2     | 29.3       |
|                | B1-2   | NA        | NA      | 2.46               | 17.7          | 65.9     | 16.4       |
|                | B1-3   | NA        | NA      | 2.31               | 21.2          | 52.6     | 26.2       |
|                | B1-4   | NA        | NA      | 2.42               | 18.6          | 56.4     | 24.9       |
|                | B1-5   | <0.01     | NA      | 2.41               | 21.2          | 65.4     | 13.4       |
|                | B2-1   | 0.15      | NA      | 2.73               | 14.3          | 70.0     | 15.7       |
|                | B2-2   | 0.01      | NA      | 2.61               | 19.1          | 64.6     | 16.2       |
|                | B2-3   | <0.01     | NA      | 2.61               | 32.7          | 56.7     | 10.6       |
|                | B2-4   | 0.23      | NA      | 2.41               | 28.9          | 53.8     | 17.2       |
|                | B2-5   | 0.11      | NA      | 2.52               | 12.6          | 76.8     | 10.6       |
| Sr2020         | B1-1   | 0.08      | 12.10   | 2.53               | 19.7          | 59.8     | 20.5       |
|                | B1-2   | <0.01     | 7.73    | 2.55               | 12.6          | 54.6     | 32.8       |
|                | B1-3   | <0.01     | 9.03    | 2.49               | 13.4          | 48.0     | 38.6       |
|                | B1-4   | <0.01     | 12.00   | 2.49               | 20.3          | 45.1     | 34.6       |
|                | B1-5   | <0.01     | 13.39   | 2.45               | 26.8          | 59.7     | 13.5       |
|                | B1-6   | <0.01     | 12.77   | 2.51               | 5.8           | 59.0     | 35.2       |
|                | B1-7   | <0.01     | 9.79    | 2.45               | 13.7          | 42.0     | 44.4       |
|                | B1-8   | <0.01     | 11.30   | 2.54               | 18.8          | 53.7     | 27.5       |
|                | B1-9   | <0.01     | 12.05   | 2.55               | 16.2          | 60.6     | 23.2       |
|                | B2-1   | 0.21      | 16.31   | 2.42               | 12.1          | 52.5     | 35.4       |
|                | B2-2   | 0.53      | 10.53   | 2.52               | 17.1          | 68.0     | 14.9       |
|                | B2-3   | 0.31      | 12.71   | 2.50               | 22.0          | 56.7     | 21.3       |
|                | B2-4   | 0.09      | 10.15   | 2.47               | 17.1          | 59.4     | 23.5       |
|                | B2-5   | 0.58      | 11.29   | 2.45               | 14.3          | 59.2     | 26.5       |
|                | B2-6   | 0.17      | 9.68    | 2.50               | 22.5          | 59.6     | 17.9       |
|                | B2-7   | 0.16      | 17.99   | 2.35               | 11.6          | 54.5     | 33.8       |
|                | B2-8   | 0.06      | 8.95    | 2.44               | 19.6          | 51.7     | 28.7       |
|                | B2-9   | 0.11      | 7.73    | 2.53               | 17.4          | 59.0     | 23.6       |
|                | B2-10  | 0.10      | 12.28   | 2.50               | 14.3          | 69.9     | 15.8       |
| Sn2020         | B1-1   | <0.01     | 13.99   | 2.50               | 17.0          | 65.6     | 17.4       |
|                | B1-2   | <0.01     | 7.89    | 2.56               | 25.2          | 58.4     | 16.5       |
|                | B1-3   | <0.01     | 15.74   | 2.55               | 25.1          | 61.0     | 13.8       |
|                | B1-4   | <0.01     | 8.82    | 2.59               | 29.0          | 58.9     | 12.1       |
|                | B1-5   | <0.01     | 5.31    | 2.65               | 29.2          | 56.2     | 14.7       |

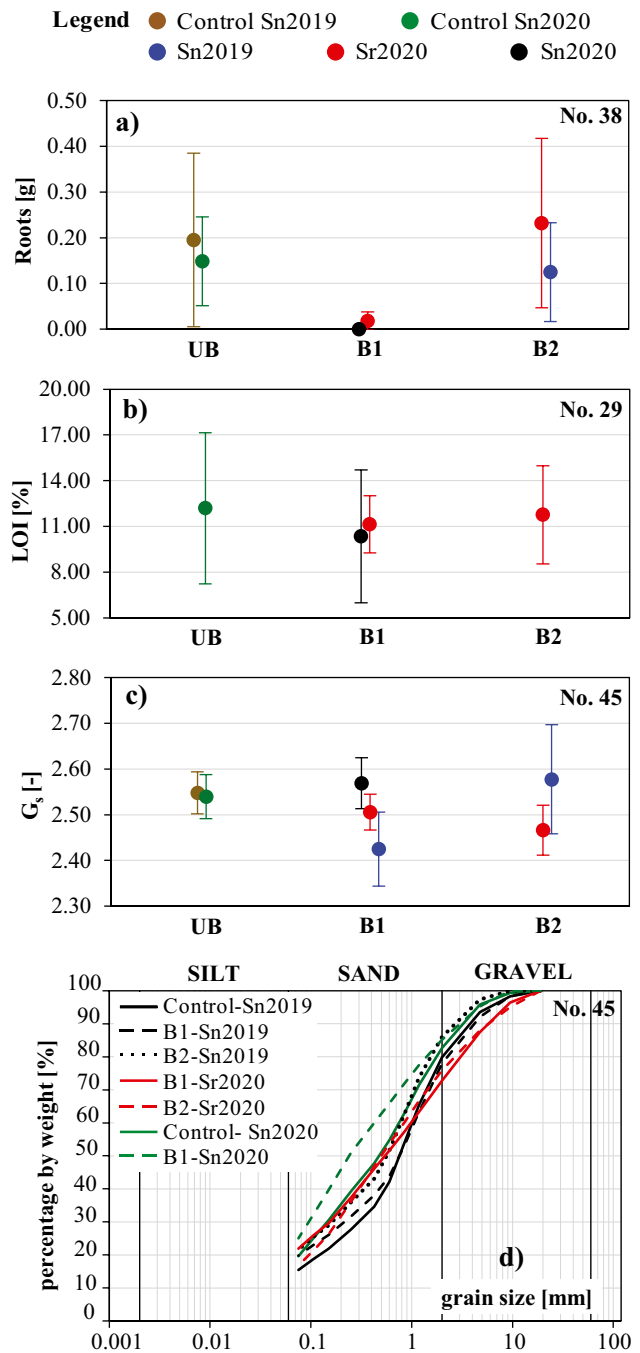


**Fig. 5** Main physical properties of the tested soil samples **a** roots; **b** loss on ignition (LOI); **c** specific gravity (G<sub>s</sub>); **d** average grain size distribution curves (GSDCs), of the soil samples for each test site and soil class (i.e., UB unburned samples, B1 burned samples collected

soon after the fires, B2 burned samples collected 5 months and 8 months after the Sn2019 and Sr2020 wildfires, respectively). “NA” in the table indicates that the corresponding information is not available, whereas “No.” is the number of tested samples

average either over time (B1, gravel = 30%, sand = 54%, silt = 16%; B2, gravel = 24%, sand = 59%, silt = 17%) or because of the fire (UB, gravel = 20%, sand = 65%, silt = 15%; B1, gravel = 15%, sand = 60%, silt = 25%), resulting also as silt in sand (MS).

**Soil mechanical properties**

Table 2 and Fig. 6 show the results of the DS tests. In general, the effect of fire consisted mainly of a decrease in the cohesive contribution to the soil shear strength.

**Table 2** DS tests results

| Test site             | Sample <sup>a</sup> | $n_i^b$<br>[-] | $n_c^c$<br>[-] | $n_r^d$<br>[-] | $\sigma_{vf}^e$<br>[kPa] | $\tau_f^f$<br>[kPa] |
|-----------------------|---------------------|----------------|----------------|----------------|--------------------------|---------------------|
| <b>Control Sn2019</b> | <b>UB-1</b>         | 0.69           | 0.69           | 0.70           | 10.6                     | 12.9                |
|                       | <b>UB-2</b>         | 0.62           | 0.62           | 0.63           | 10.6                     | 11.7                |
|                       | <b>UB-3</b>         | 0.71           | 0.71           | 0.72           | 10.6                     | 12.5                |
|                       | <b>UB-4</b>         | 0.66           | 0.66           | 0.67           | 17.7                     | 17.1                |
|                       | <b>UB-5</b>         | 0.59           | 0.58           | 0.60           | 34.2                     | 29.2                |
| <b>Control Sn2020</b> | <b>UB-6</b>         | 0.61           | 0.61           | 0.62           | 10.6                     | 10.4                |
|                       | <b>UB-7</b>         | 0.62           | 0.62           | 0.63           | 17.7                     | 17.5                |
|                       | <b>UB-8</b>         | 0.72           | 0.71           | 0.72           | 34.2                     | 33.0                |
|                       | <b>UB-9</b>         | 0.70           | 0.70           | 0.72           | 10.6                     | 14.6                |
|                       | <b>UB-10</b>        | 0.61           | 0.61           | 0.63           | 17.7                     | 18.3                |
| <b>Sn2019</b>         | <b>B1-1</b>         | 0.67           | 0.67           | 0.68           | 10.6                     | 10.4                |
|                       | <b>B1-2</b>         | 0.64           | 0.64           | 0.63           | 17.7                     | 16.1                |
|                       | <b>B1-3</b>         | 0.68           | 0.66           | 0.67           | 23.5                     | 20.4                |
|                       | <b>B1-4</b>         | 0.67           | 0.66           | 0.66           | 34.2                     | 27.0                |
|                       | <b>B2-1</b>         | 0.53           | 0.53           | 0.52           | 10.6                     | 10.4                |
|                       | <b>B2-2</b>         | 0.64           | 0.64           | 0.64           | 17.7                     | 15.4                |
|                       | <b>B2-3</b>         | 0.65           | 0.64           | 0.64           | 23.5                     | 20.0                |
|                       | <b>B2-4</b>         | 0.64           | 0.63           | 0.62           | 34.2                     | 26.7                |
| <b>Sr2020</b>         | <b>B1-1</b>         | 0.68           | 0.68           | 0.69           | 10.6                     | 14.6                |
|                       | <b>B1-4</b>         | 0.69           | 0.69           | 0.73           | 10.6                     | 12.5                |
|                       | <b>B1-5</b>         | 0.71           | 0.70           | 0.70           | 17.7                     | 14.2                |
|                       | <b>B1-6</b>         | 0.65           | 0.64           | 0.64           | 34.1                     | 27.9                |
|                       | <b>B1-9</b>         | 0.67           | 0.66           | 0.66           | 34.1                     | 31.3                |
|                       | <b>B2-1</b>         | 0.74           | 0.74           | 0.76           | 10.6                     | 14.6                |
|                       | <b>B2-4</b>         | 0.65           | 0.64           | 0.66           | 10.6                     | 12.9                |
|                       | <b>B2-6</b>         | 0.64           | 0.63           | 0.63           | 34.1                     | 28.3                |
|                       | <b>B2-7</b>         | 0.71           | 0.70           | 0.73           | 10.6                     | 13.3                |
|                       | <b>B2-8</b>         | 0.63           | 0.62           | 0.63           | 17.7                     | 20.8                |
| <b>Sn2020</b>         | <b>B1-2</b>         | 0.63           | 0.63           | 0.64           | 10.6                     | 11.7                |
|                       | <b>B1-3</b>         | 0.72           | 0.72           | 0.73           | 17.7                     | 15.8                |
|                       | <b>B1-4</b>         | 0.64           | 0.63           | 0.64           | 34.1                     | 31.7                |

<sup>a</sup>soil material

<sup>b</sup>value of porosity before the consolidation stage

<sup>c</sup>value of porosity at the end of the consolidation stage

<sup>d</sup>value of porosity at the end of the shear stage

<sup>e</sup>vertical stress at failure

<sup>f</sup>shear stress at failure

The Sn2019 (Fig. 6a) B1 samples show a decrease in cohesion compared to the corresponding UB, from  $c = 4.7$  kPa to the value of  $c = 3.4$  kPa. In contrast, the friction angle almost does not change ( $35.5^\circ$  for UB to  $35.1^\circ$  for B1). Samples collected five months after the fire event (B2) exhibit cohesion and friction angle of 3.3 kPa and  $34.7^\circ$ , respectively, thus not recovering the cohesion of the UB samples and keeping the friction angle almost unchanged.

Regarding the Sr2020 site (Fig. 6b), the samples collected eight months after the fire event (B2) show higher

cohesion than those collected soon after the fire (B1). In particular, a shift from a cohesion of 4.9 kPa to 6.7 kPa occurs. In addition, also in this case, the friction angle remains almost unchanged over time (i.e.,  $35.3^\circ$  for B1 and  $34.6^\circ$  for B2).

The samples of the Sn2020 site (Fig. 6c) reveal the same trend as the other two case studies. Indeed, the cohesion ranges from 3 kPa for the UB samples to 1.6 kPa for the B1, whereas the friction angle is almost kept constant (i.e.,  $41.1^\circ$  for UB and  $41.0^\circ$  for B1).

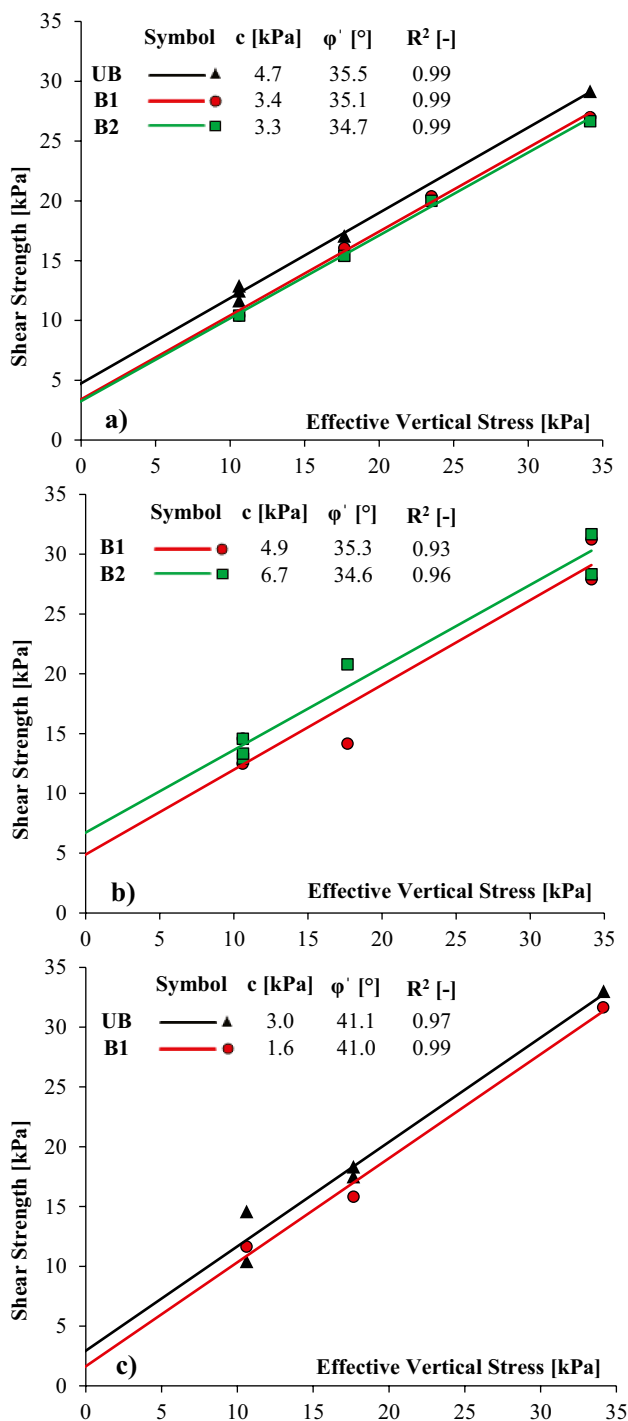


**Fig. 6** DS tests results in terms of shear strength envelopes for the a Sn2019, b Sr2020, c Sn2020 soil samples (i.e., UB unburned samples, B1 burned samples collected soon after the fires, B2 burned samples collected 5 months and 8 months after the Sn2019 and Sr2020 wildfires, respectively). “c”, “ $\phi'$ ”, and “R<sup>2</sup>” are the soil cohesion, effective friction angle, and coefficient of determination of the failure envelopes, respectively

## Soil hydraulic properties

Figure 7a shows the trends of the SWRCs obtained from the suction-controlled oedometer tests on undisturbed soil samples initially saturated and then subjected to a continuously drying process.

Overall, the hydraulic behaviors seem to depend on the characteristics of the specific burned site and its burn severity.

Concerning the Sn2019 site, the B1 sample exhibits lower volumetric water content ( $\theta_w$ ) than the corresponding B2 up to matric suction of 10 kPa. Beyond this value, no significant deviations in  $\theta_w$  appear between the two sample classes. Thus, in this case, the fire effect is significant at low matric suction levels.

As for the Sr2020 site, similar values of  $\theta_w$  are recorded between the B1 and B2 samples up to matric suction of 1 kPa; after this value, the SWRC of the B1 sample tends to deviate from that of the B2 sample, showing a higher  $\theta_w$  at given matric suction.

In this work, a significant increase in air-entry value (AEV) and n parameter between the B1 and B2 samples of the Sn2019 site is noticed (from 1.93 to 4.08 kPa and from 1.44 to 2.21, respectively), whereas the Sr2020 keeps AEV and n values almost unchanged (from 1.06 to 1.10 kPa and from 1.14 to 1.36, respectively).

The general trends of the HCFs show increases in the permeability coefficient (K) for the B2 samples compared to the B1 samples, mainly in the range of matric suction between 0.01 and 30 kPa (Fig. 7b). At higher matric suction values, no significant changes are observed. However, the change in the permeability coefficient seems more significant for the Sn2019 sample, which is characterized by a maximum increase of K (between B1 and B2) of  $1.07\text{E-}03$  cm/s (at 0.2 kPa matric suction), whereas the maximum increase for the Sr2020 sample is  $9.32\text{E-}04$  cm/s (at 0.01 kPa matric suction).

Eventually, the  $K_s$  value of the B1 sample ( $3.30 \times 10^{-4}$  cm/s) is lower than the B2 ( $1.28 \times 10^{-3}$  cm/s).

## Discussion

Laboratory test results provided insights into the post-fire physical and hydromechanical properties of pyroclastic soils collected from three sites affected by wildfires in 2019 and 2020. In general, the fire-induced changes in soil properties were highly site-specific due to the intrinsic variability of the tested soils and the different burn severity of the fires.

|           |        | Samples Characteristics |                               |                |                    |                |                    |                   | Van Genuchten's Model (VG) - Hydraulic Parameters |   |                                 |            |              |
|-----------|--------|-------------------------|-------------------------------|----------------|--------------------|----------------|--------------------|-------------------|---|---|---------------------------------|------------|--------------|
| Test Site | Sample | $H_1^1$<br>[cm]         | $V_1^2$<br>[cm <sup>3</sup> ] | $n_0^3$<br>[-] | $S_{r,0}^4$<br>[-] | $n_r^5$<br>[-] | $S_{r,r}^6$<br>[-] | $K_s^7$<br>[cm/s] | $\theta_s$<br>[cm <sup>3</sup> cm <sup>-3</sup> ] | $\theta_r$<br>[cm <sup>3</sup> cm <sup>-3</sup> ] | $\alpha$<br>[cm <sup>-1</sup> ] | $n$<br>[-] | $R^2$<br>[-] |
| Sn2019    | B1-5   | 2.00                    | 49.26                         | 0.69           | 0.61               | 0.68           | 0.32               | 3.30E-04          | 0.693   | 0.212   | 0.614                           | 1.444      | 0.99         |
|           | B2-5   | 2.00                    | 49.26                         | 0.70           | 0.29               | 0.70           | 0.31               | 1.28E-03          | 0.711   | 0.298   | 0.245                           | 2.214      | 0.99         |
| Sr2020    | B1-9   | 2.00                    | 49.26                         | 0.68           | 0.35               | 0.67           | 0.26               | 3.30E-04          | 0.681   | 0.000   | 0.942                           | 1.144      | 1.00         |
|           | B2-10  | 2.00                    | 49.26                         | 0.69           | 0.40               | 0.69           | 0.33               | 1.28E-03          | 0.687   | 0.212   | 0.905                           | 1.361      | 0.99         |

<sup>1</sup>specimen height <sup>2</sup>specimen volume after the saturation <sup>3</sup>porosity value before the saturation <sup>4</sup>degree of saturation before the saturation <sup>5</sup>porosity value at the end of the test <sup>6</sup>degree of saturation at the end of the test <sup>7</sup>saturated hydraulic conductivity

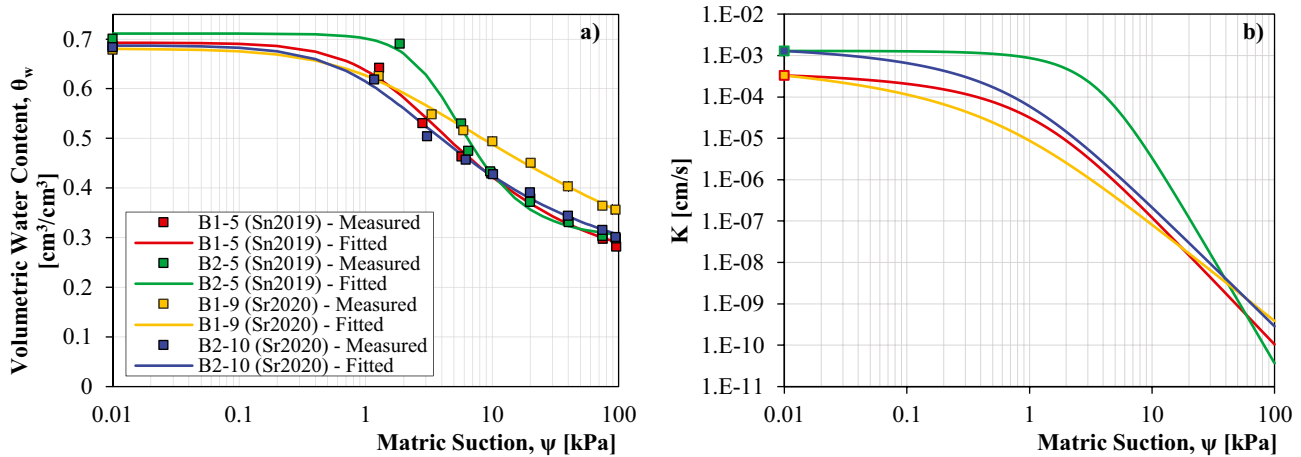


Fig. 7 a SWRCs and b HCFs of the investigated soil samples

Qualitative in situ assessment of ground cover and soil structure revealed that the Sn2019 site did not exhibit significant fire-induced changes compared to the corresponding unburned control site (Control Sn2019) (Table 1). The main effects were the deposition of partially burned residual material (e.g., leaves, charcoal) and the scorching of topsoil roots. This evidence may be because the ground cover was sparse before the fire, so there was not enough fuel to maintain the heat for a sufficient time to significantly affect the SOM. On the other hand, the Sr2020 and Sn2020 burned sites were characterized by significant changes in ground cover, soil structure, and root condition. Here, the fires caused the removal of 75% of the vegetation, the burning of organic material in the surface soil horizon, and the almost complete combustion of fine roots (Table 1). The Sr2020 and Sn2020 sites were also characterized by the deposition of post-fire residual material above the topsoil layer, distinguished by ash colors ranging from black/gray to white with a thickness of 5–6 cm (Fig. 4).

As extensively demonstrated in the literature, all the documented changes may play a relevant role in triggering post-fire runoff and erosion processes (Woods and Balfour 2008). Loss or reduction of effective ground cover is a key factor in reducing soil roughness and infiltration capacity while increasing soil erodibility and the risk of overland flow generation (Moody et al. 2013; Rengers et al. 2020).

The organic compounds can also act as an adhesive that binds soil particles into stable aggregates that resist detachment (Mataix-Solera et al. 2011). Depending on soil type and degree of heating, exposed soils may become loose and thus more susceptible to detachment by wind, water, and gravity (Parsons et al. 2010). In addition, previous studies suggest that ash may wash or infiltrate into the soil, clogging soil pores and limiting infiltration rates, resulting in increased soil–water retention and decreased soil hydraulic conductivity (Mallik et al. 1984; Woods and Balfour 2006; Lei et al. 2022).

Regarding soil physical properties (Fig. 5), no significant change was observed in the GSD of burned samples (B1) compared to the corresponding unburned (UB) or revegetated (B2) samples of the three sites, in agreement with the findings of Esposito et al. (2017), who showed that the textural classes of the pyroclastic soils in the same study area were not significantly affected by a fire in 2012. However, it is worth noting that several studies report both increases (Ulery and Graham 1993; González-Pérez et al. 2004; Terefe et al. 2008; Granged et al. 2011) and decreases (Stoof et al. 2010) in GSD as a consequence of fire. In general, the increases in the average GSD are linked to the aggregation of finer clay particles into stable silt- and sand-sized particles. Depending on soil type, Granged et al. (2011) explained the increment of the coarser fraction observed immediately after a fire by

the calcination of iron and aluminosilicates at temperatures near 300 °C, whereas Ulery and Graham (1993) and Terefe et al. (2008) attributed the increase of the sand fraction to the aluminum oxides and hydroxides released during the clay decomposition, which may act as cementing agents in the formation of sand-sized particles. On the other hand, the decreases in GSD are found in literature as a result of the physical weathering of the sand-sized particles into silt- and clay-sized particles due to heating and burning (Stoof et al. 2010). Based on the previous remarks, it is likely that none (or both) of the two above-mentioned phenomena has occurred for the case studies at hand, depending upon the specific type of investigated soil (i.e., pyroclastic and coarse-grained) as well as the thermal conditions reached during the fire events.

Figure 8 plots  $G_s$  against LOI calculated for the samples of Sr2020 and Sn2020 fire sites. The black dashed line indicates the general trend consisting of a decrease in  $G_s$  as LOI increases. Such a trend can be explained by the SOM that, as verified during the field surveys, was mainly formed by roots, soil aggregates, and fire residues (e.g., ash and charcoal), resulting in lighter than mineral particles and taking up a larger volume at fixed weight. Therefore, as LOI increases, the SOM content also increases with respect to the mineral content of the soil. Generally, the value of LOI is not significantly changed among the sample classes of each test site (Fig. 5). In contrast, the type of SOM varied because it strictly depends on the type of soil, vegetation, and the specific soil burn severity (i.e., the degree of combustion

reached by the particular type of SOM). Indeed, a severe fire can leave highly combusted organic matter, depending on its duration and intensity. The Sn2019 B1 samples were characterized mainly by fire residues partially or not at all burned by the low burn severity fire (e.g., leaves and charcoal), whereas the Sr2020 and Sn2020 B1 samples exhibited layers of post-fire residual material on the topsoil distinguished by a high degree of combustion. In the light of this, data related to samples of the Sr2020 and Sn2020 fire sites do not display significant changes in LOI and  $G_s$  between the B1 samples and the B2/UB samples (Fig. 5b, c), respectively. The burn severity of these fires was moderate-high and a severe level of combustion characterized the post-fire residues that, for this reason, assumed a negligible weight. In contrast, for the Sn2019 fire site (Fig. 5c), we found a reduction in  $G_s$  caused by the fire (on average, from 2.55 for UB to 2.42 for B1). We assume that this decrease in  $G_s$  was due to the deposition of fire residues characterized by a lower degree of combustion than those of the Sr2020 and Sn2020 sites and, consequently, a higher volume. Indeed, as evidence of this, the samples collected five months after the fire event (B2) showed an average  $G_s$  value similar to the unburned samples (UB) since most of the post-fire residues were removed from the topsoil layer as a result of post-fire erosive processes mainly driven by intense rainfall (Fig. 2).

Overall, the average RCW was lower in the B1 samples compared to the UB and B2 samples (Fig. 5a). From the field surveys, we observed that the soil roots had been partially or totally burned by the heat produced during the fires, leading to negative impacts on soil cohesion.

In particular, concerning changes in soil mechanical properties, a general reduction in the cohesive contribution of B1 versus UB and B2 samples was found (Figs. 6 and 9). This was mostly due to the fire-induced roots combustion and weakening in the B1 samples. In particular, the investigated soils are loose and of pyroclastic origin, in a way that only their root systems and SOM aggregates may provide a cohesive contribution under saturated conditions (Foresta et al. 2020). The results reveal that fire can weaken surficial roots, reducing the associated contribution to the soil shear strength, leaving the soil more prone to saturate and thus reach the critical strength of failure. In turn, this leads to the frequent occurrence of post-fire landslides and debris flows. In addition, soil shear strength may be increased/recovered after a variable time, strictly dependent on the specific site (i.e., roots) and fire conditions. In this regard, detailed long-time observation and research concerning the relationship between the post-fire temporal evolution of the vegetation state (mainly roots condition) and the geotechnical properties of the affected soil are necessary to improve the knowledge on the mechanisms of post-fire landslides.

Moreover, our results highlight that the higher shear strength of unburned and revegetated samples compared to burned

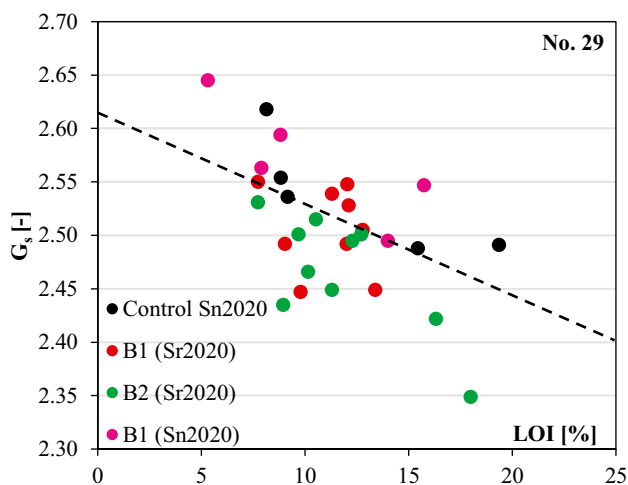


**Fig. 8** Specific gravity ( $G_s$ ) vs. loss on ignition (LOI) of each site and soil sample class (i.e., Control Sn2020: unburned samples of the Sn2020 Fire site, B1 (Sr2020): burned samples collected soon after the Sr2020 fire, B2 (Sr2020): burned samples collected 8 months after the Sr2020 wildfire, B1 (Sn2020) burned samples collected soon after the Sn2020 fire). The black dashed line indicates the general trend of  $G_s$  vs. LOI, obtained considering all the samples whose  $G_s$  and LOI data were available. “No.” is the number of tested samples

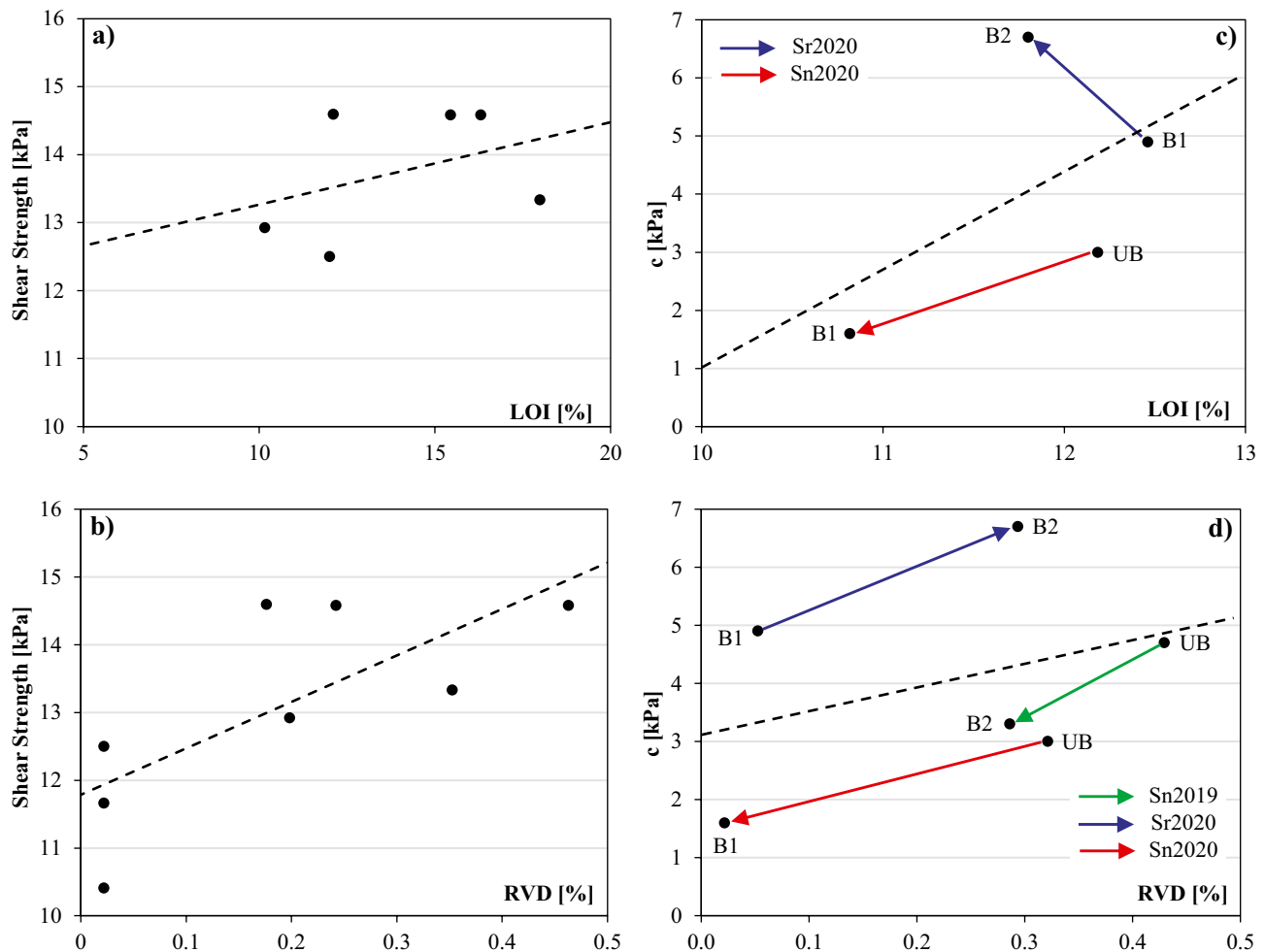


**Fig. 9** Soil shear stress vs. **a** loss on ignition (LOI), **b** root volume density (RVD); soil cohesion (c) vs. **c** LOI, **d** root volume density (RVD). The black dashed lines represent the general trends

(UB unburned samples, B1 burned samples collected soon after the fires, B2 burned samples collected 5 months and 8 months after the Sn2019 and Sr2020 wildfires, respectively)

samples seems mainly due to root content rather than SOM (as it is related to LOI values) (Fig. 9a, b). As confirming evidence of this, with reference to the Sr2020 fire, Fig. 9c shows an increase in cohesion for the B2 samples with a reduction in LOI (i.e., potentially lower SOM content due to runoff). In contrast, Fig. 9d shows that as root content increases, cohesion always increases. Furthermore, since the investigated topsoil is highly heterogeneous and site-specific, it is worthwhile to analyze the results for individual test sites (Fig. 9). The B1 samples of the Sr2020 and Sn2020 fire sites show lower cohesion values than the corresponding B2 and UB samples, respectively (Fig. 9c, d). The latter are characterized by higher average RCW, with no significant differences in LOI. Therefore, in this case, the higher cohesion for the B2 and UB samples may depend on the contribution to shear strength provided by the root systems, which is reduced for the B1 samples due to the fire-induced scorching and weakening of roots. Similarly, the Sn2019 fire produced root burning and weakening, decreasing the cohesion of the B1

and B2 samples compared to corresponding UB samples. Thus, in this case, the cohesion did not change five months after the B1 sampling. Here, we show that even a low burn severity fire can potentially reduce the cohesion of the topsoil layer, and this weakening of mechanical strength can persist for a considerable time following a fire, during which the triggering of post-fire debris flows is possible (e.g., McGuire et al. 2021).

Several researchers have found that roots can lose strength following a fire, thereby reducing their cohesive contribution, leaving hillslopes more prone to failure (Regelbrugge and Conard 1993; Jackson and Roering 2009; De Graff 2018; Gehring et al. 2019; Lei et al. 2022). The key role of vegetation in stabilizing hillsides is well known (Löbmann et al. 2020). Living plants can increase soil shear strength via mechanical effects and evapotranspiration-induced suction (Bordoloi and Ng 2020). Here, we found that plant roots tend to increase the shear strength of soil primarily by increasing the soil cohesion, which is consistent with the

literature studies on the topic (e.g., Wu 2013). In addition, we showed that the recovery/increase in soil shear strength depends on time and the specific site/fire conditions. Moreover, the tested sample classes are characterized by a fine-grained fraction ranging between about 15% and 25%, which may have affected the obtained cohesion values. However, in this regard, we assume that the cohesion values found are due to the presence of root systems rather than the amount of fine-grained fraction, given that the tested soils are characterized by being granular, loose, and cohesionless (Comegna and Damiano 2016; Olivares et al. 2018).

In this work, the hydrological response to a continuous drying process of initially saturated soil samples collected in the Sn2019 and Sr2020 fire sites was investigated to examine the effects of fire on the soil hydraulic properties (Fig. 7).

The B1 samples from the two sites showed lower saturated hydraulic conductivity ( $K_s$ ) compared to the corresponding B2 samples. We suggest that this difference in  $K_s$  was likely due to the phenomenon of post-fire residues clogging soil pores for the B1 samples (Woods and Balfour 2010) and to the change in the macropore flow paths for the B2 samples (Nyman et al. 2014), which were characterized by higher RCW.

The SWRCs of the B2 samples exhibited different behaviors for the Sn2019 and Sr2020 fire sites compared to the corresponding B1 samples. In particular, the B2 sample of the Sn2019 site showed increases in volumetric water content at low matric suction values (up to 10 kPa). In contrast, the B2 sample of the Sr2020 site was characterized by decreased volumetric water content over most of the range of matric suction investigated (between 2 and 100 kPa). The different behaviors between the B2 samples of the two test sites may be due to the different burn severity of the fires, which may have resulted in different effects on the factors that affect soil–water retention capacity.

Generally, fires in the study area occur during the dry period (late summer-early autumn) when vegetation moisture conditions and weather are favorable factors for the ignition and subsequent spread of fires. To properly understand the triggering mechanism of the post-fire events that occurred at the three test sites, it is helpful to compare the rainfall intensity with the  $K_s$  of the tested soil samples (i.e., B1 and B2).  $K_s$  is an important soil characteristic affecting soil water storage, runoff generation, and erosion. Overland flows are frequent in burned areas where rainfall intensity exceeds the  $K_s$  values at shallow soil depths (e.g., De Bano 2000), according to the Hortonian mechanism (Horton 1932). In contrast, if the rainfall intensity is less than the  $K_s$  of the surface soil, all the water will infiltrate into the soil, and runoff will not be generated. The 10-min peak storm intensities ( $I_{10}$ ) characterizing the rainstorms that triggered the post-fire events (i.e., hyperconcentrated and debris flows) in November 2019 and September 2020 were

50 and 102 mm/h, respectively. The average storm intensities resulted in 25.2 and 51 mm/h. On the other hand, the  $K_s$  of the considered B1 and B2 samples were 11.8 and 46.8 mm/h, respectively. Thus, by comparing the rainfall intensities with the  $K_s$ , we verified that conditions leading to the Hortonian infiltration-excess mechanism would have occurred in both cases. However, erosion responses were recorded only after the B1 sampling (i.e., not after the B2 sampling). Therefore, besides the decreased hydraulic conductivity and the decreased cohesion of the topsoil, we suppose that the triggering of post-fire overland flows may have been favored by the loss of vegetation cover and the deposition of post-fire residues (e.g., charcoal, ash). This issue deserves to be fully investigated with in situ analyses in the follow-up of this research. In addition, further future studies on fire-induced changes in soil properties, as well as long-time and continuous observation data and research, will further help reveal the starting mechanism of post-fire events.

In the present work, we have assumed that the SWRCs obtained through wetting path are likely to be characterized by lower values of volumetric water content compared to the SWRCs derived following a drying path, as well as by the same shape, regardless of the specific sample class considered (i.e., burned or revegetated samples). Indeed, Leung et al. (2015), who studied the hysteretic behavior of rooted and bare soil samples, showed that the shape of the SWRC in wetting path is unchanged, regardless of the actual sample class. This evidence led us to assume that burned samples (seen as bare soil samples) and unburned samples (seen as rooted soil samples), besides exhibiting water content or coefficient of permeability values always lower than those found on the associated drying curve, are also likely to be characterized by the same shape of the SWRC in wetting path. This would result in lower  $K$  values for the wetting curve, associated with an increased runoff and erosion rates. On the same line, Comegna et al. (2016) have investigated the influence of potential wetting paths on virtual slope stability conditions, stressing the potential errors in the prediction of landslide triggering, which might be associated with the use of a unique SWRC assumed to simplify the wetting paths. In particular, along scanning curves, they have highlighted that a quicker water content change than found in other paths could take place; therefore, under critical precipitation the time to failure could be shorter than expected.

## Conclusions

The data presented in this study document the physical and hydromechanical properties of pyroclastic soils collected from three test sites that suffered wildfires and rainfall-induced post-fire events in 2019 and 2020.



The results revealed to be site-specific, mainly depending on soil characteristics and fire burn severity.

Regarding the soil physical properties, no significant changes were found in the grain size distribution, SOM, and specific gravity of burned compared to unburned and revegetated samples.

Moreover, the results from the DS tests demonstrated degradation of the soil mechanical properties because of the wildfires. In particular, a decrease in soil cohesion was observed due to fire burning and weakening of the root systems. We found that even a low burn severity fire can cause a decrease in soil cohesion, and recovery of this contribution is possible, mainly depending on site conditions, burn severity, and time after the fire. In addition, no change in soil friction angle due to fire was found.

Regarding soil hydraulic properties, the burned samples exhibited soil water retention and hydraulic conductivity changes under both saturated and unsaturated conditions. Specifically, a decrease in the hydraulic conductivity of burned soils compared to revegetated samples was found.

We infer that the documented post-fire erosion responses have been mainly fostered by the reduced cohesion and hydraulic conductivity of the burned topsoil layer, along with the loss of vegetation cover and the deposition of post-fire residues, as observed by many authors worldwide.

These findings provide important insights into the changes in physical and hydromechanical properties of fire-affected pyroclastic soils. They represent a key for understanding the initiation mechanism of post-fire debris flows.

Bearing in mind the lack of information on the effects of fire on the physical-hydro-mechanical properties of pyroclastic soils, the presented study – although deserving further deepening – may represent a starting point to provide input data to stability analyses aimed at assessing the possible increase of the susceptibility to slope instability processes over several natural slopes that are in the same conditions as the ones here analyzed.

**Author contribution** Conceptualization, D.P., L.I., G.E., V.F. and F.M.; investigation, L.I.; methodology, D.P., L.I. and V.F.; supervision, D.P., G.E., V.F. and F.M.; writing–original draft, L.I.; writing–review and editing, D.P., V.F. and F.M.; Sect. 2.2, G.E. and R.M. All authors have read and agreed to the published version of the manuscript.

**Funding** Open access funding provided by Università degli Studi di Salerno within the CRUI-CARE Agreement.

## Declarations

**Competing interests** The authors declare no competing interests.

**Open Access** This article is licensed under a Creative Commons Attribution 4.0 International License, which permits use, sharing, adaptation, distribution and reproduction in any medium or format, as long

as you give appropriate credit to the original author(s) and the source, provide a link to the Creative Commons licence, and indicate if changes were made. The images or other third party material in this article are included in the article's Creative Commons licence, unless indicated otherwise in a credit line to the material. If material is not included in the article's Creative Commons licence and your intended use is not permitted by statutory regulation or exceeds the permitted use, you will need to obtain permission directly from the copyright holder. To view a copy of this licence, visit <http://creativecommons.org/licenses/by/4.0/>.

## References

- Alauzis MV, Mazzarino MJ, Raffaele E, Roselli L (2004) Wildfires in NW Patagonia: long term effects on a *Nothofagus* forest soil. *For Ecol Manage* 192:131–142
- ASTM D 854 (2014) Standard Test Methods for Specific Gravity of Soil Solids by Water Pycnometer, ASTM International, West Conshohocken, PA. [www.astm.org](http://www.astm.org). Accessed 15 Feb 2022
- ASTM D3080 (2011) Direct Shear Test of Soils under Consolidated Drained Conditions, ASTM International, West Conshohocken, PA. [www.astm.org](http://www.astm.org). Accessed 15 Feb 2022
- ASTM D422–63 (2007) Standard Test Method for Particle-Size Analysis of Soils, ASTM International, West Conshohocken, PA. [www.astm.org](http://www.astm.org). Accessed 15 Feb 2022
- ASTM D7348–08 (2011) Standard Test Methods for Loss on Ignition (LOI) of Solid Combustion Residues, ASTM International, West Conshohocken, PA. [www.astm.org](http://www.astm.org). Accessed 15 Feb 2022
- Aversa S, Nicotera MV (2002) A triaxial and oedometer apparatus for testing unsaturated soils. *Geotech Test J* 25:3–15. <https://doi.org/10.1520/gtj11075j>
- Badía D, Martí C (2003) Plant ash and heat intensity effects on chemical and physical properties of two contrasting soils. *Arid L Res Manag* 17:23–41. <https://doi.org/10.1080/15324980301595>
- Benda L, Miller D, Bigelow P, Andras K (2003) Effects of post-wildfire erosion on channel environments, Boise River, Idaho. *For Ecol Manage* 178:105–119. [https://doi.org/10.1016/S0378-1127\(03\)00056-2](https://doi.org/10.1016/S0378-1127(03)00056-2)
- Bengtsson L, Enell M (1986) Chemical analysis. In: Berglund BE (ed) *Handbook of Holocene Paleoecology and Palaeohydrology*. Wiley, Chichester, pp 423–445
- Bilotta E, Cascini L, Foresta V, Sorbinow G (2005) Geotechnical characterisation of pyroclastic soils involved in huge flowslides. *Geotech Geol Eng* 23:365–402. <https://doi.org/10.1007/s10706-004-1607-3>
- Bordoloi S, Ng CWW (2020) The effects of vegetation traits and their stability functions in bio-engineered slopes: A perspective review. *Eng Geol* 275:105742. <https://doi.org/10.1016/j.enggeo.2020.105742>
- Brondi F, Salvatori L (2003) The 5–6 May 1998 mudflows in Campania, Italy. In: Hervás J (ed) *Lessons learnt from landslide disasters in Europe*. European Commission Joint Research Centre, Institute for Environment and Sustainability, pp 5–16 (NEDIES Project – Report EUR 20558 EN)
- Calcaterra D, Parise M, Palma B, Pelella L (2000) The influence of meteoric events in triggering shallow landslides in pyroclastic deposits of Campania, Italy. *Landslides in Research, Theory and Practice: Proceedings of the 8th International Symposium on Landslides*, vol 1. Cardiff, pp 209–214, 26–30 Jun 2000
- Cascini L, Cuomo S, Della Sala M (2011) Spatial and temporal occurrence of rainfall-induced shallow landslides of flow type: a case of Sarno-Quindici, Italy. *Geomorphology* 126:148–158. <https://doi.org/10.1016/j.geomorph.2010.10.038>

- Cascini L, Ferlisi S, Vitolo E (2008) Individual and societal risk owing to landslides in the Campania region (Southern Italy). *Georisk* 2:125–140. <https://doi.org/10.1080/17499510802291310>
- Cascini L, Guida D, Nocera N, Romanzi G, Sorbino G (2000) A preliminary model for the landslides of May 1998 in Campania Region. *Proc 2nd Int. Symposium on Geotechnics of Hard Soil-Soft Rock*, vol 3. Balkema, Napoli, pp 1623–1649
- Cascini L, Sorbino G (2002) Soil suction measurement over large areas: a case study. In: Juca J, de Campos T, Marinho F (eds) *Proceedings of the 3rd International Conference on Unsaturated Soils, UNSAT 2002*. CRC Press, Recife, Brazil, pp 829–834
- Chen P, Ning L, Wei C (2019) General scanning hysteresis model for soil-water retention curves. *J Geotech Geoenviron Eng* 145(12):04019116. [https://doi.org/10.1061/\(ASCE\)GT.1943-5606.0002184](https://doi.org/10.1061/(ASCE)GT.1943-5606.0002184)
- Comegna L, Damiano E (2016) Influence of the antecedent long-term precipitations on the initial conditions in a sloping pyroclastic deposit. *Proced Earth Planet Sci* 16:108–117. <https://doi.org/10.1016/j.proeps.2016.10.012>
- Comegna L, Damiano E, Greco R, Olivares L, Picarelli L (2021) The hysteretic response of a shallow pyroclastic deposit. *Earth Syst Sci Data* 13(6):2541–2553. <https://doi.org/10.5194/essd-13-2541-2021>
- Comegna L, Rianna G, Lee S, Picarelli L (2016) Influence of the wetting path on the mechanical response of shallow unsaturated sloping covers. *Comput Geotech* 73:164–169. <https://doi.org/10.1016/j.compgeo.2015.11.026>
- Crosta GB, Dal Negro P (2003) Observations and modelling of soil slip-debris flow initiation processes in pyroclastic deposits: the Sarno 1998 event. *Nat Hazard* 3:53–69. <https://doi.org/10.5194/nhess-3-53-2003>
- Cruden DM, Varnes DJ (1996) Landslide types and processes. In: Turner AK, Schuster RL (eds) *Landslides-Investigation and mitigation: Transportation Research Board. National Research Council, National Academy Press, Washington, DC*, pp 36–75 (Special report no. 247)
- Damiano E, Olivares L (2010) The role of infiltration processes in steep slope stability of pyroclastic granular soils: laboratory and numerical investigation. *Nat Hazards* 52:329–350. <https://doi.org/10.1007/s11069-009-9374-3>
- De Bano LF (2000) The role of fire and soil heating on water repellency in wildland environments: a review. *J Hydrol* 231–232:195–206
- De Graff JV (2018) A rationale for effective post-fire debris flow mitigation within forested terrain. *Geoenviron Disasters* 5:7. <https://doi.org/10.1186/s40677-018-0099-z>
- De Luca C, Furcolo P, Rossi F et al (2010) Extreme rainfall in the Mediterranean. *Proceedings of the International Workshop on Advances in Statistical Hydrology*, Taormina, Italy
- De Vita D, Agrello F, Ambrosino C (2006) Landslide susceptibility assessment in ash-fall pyroclastic deposits surrounding Mount Somma-Vesuvius: application of geophysical surveys for soil thickness mapping. *J Appl Geophys* 59:126–139
- De Vita P, Napolitano E, Godt JW, Baum RL (2013) Deterministic estimation of hydrological thresholds for shallow landslide initiation and slope stability models: case study from the Somma-Vesuvius area of southern Italy. *Landslides* 10:713–728. <https://doi.org/10.1007/s10346-012-0348-2>
- De Vita P, Nappi M (2011) Regional distribution of ash fall pyroclastic soils for landslide susceptibility assessment. *Proceedings of the Second World Landslide Forum, Rome*, 3–7 Oct 2011
- Dean WE (1974) Determination of carbonate and organic matter in calcareous sediments and sedimentary rocks by loss on ignition: comparison with other methods. *J Sediment Petrol* 44:242–248
- Di Nocera S, Matano F, Pescatore T et al (2011) Geological characteristics of the external sector of the Campania-Lucania Apennines in the CARG maps. *Rendiconti Online Societa Geologica Italiana* 12:39–43
- Esposito G, Esposito E, Matano F et al (2013) Effects of a wildfire on rocks and soils in the Sarno Mountains, Campania, Southern Apennines. *Rendiconti Online Soc Geol Ital* 24:119–121
- Esposito G, Matano F, Molisso F et al (2017) Post-fire erosion response in a watershed mantled by volcanoclastic deposits, Sarno Mountains, Southern Italy. *CATENA* 152:227–241. <https://doi.org/10.1016/j.catena.2017.01.009>
- Esposito G, Parodi A, Lagasio M et al (2019) Characterizing consecutive flooding events after the 2017 Mt. Salto Wildfires (Southern Italy): hazard and emergency management implications. *Water* 11:2663. <https://doi.org/10.3390/W11122663>
- Fernández I, Cabaneiro A, Carballas T (1997) Organic matter changes immediately after a wildfire in an Atlantic forest soil and comparison with laboratory soil heating. *Soil Biol Biochem* 29:1–11. [https://doi.org/10.1016/S0038-0717\(96\)00289-1](https://doi.org/10.1016/S0038-0717(96)00289-1)
- Foresta V, Capobianco V, Cascini L (2020) Influence of grass roots on shear strength of pyroclastic soils. *Can Geotech J* 57:1320–1334
- Fredlund DG, Rahardjo H (1993) *Soil mechanics for unsaturated soils*. John Wiley and Sons Inc, New York. <https://doi.org/10.1002/97804701172759>
- García-Corona R, Benito E, De Blas E, Varela ME (2004) Effects of heating on some soil physical properties related to its hydrological behaviour in two north-western Spanish soils. *Int J Wildl Fire* 13:195–199. <https://doi.org/10.1071/WF03068>
- Gehring E, Conedera M, Maringer J et al (2019) Shallow landslide disposition in burnt European beech (*Fagus sylvatica* L.) forests. *Sci Rep* 9:1–11. <https://doi.org/10.1038/s41598-019-45073-7>
- González-Pérez JA, González-Vila FJ, Almendros G, Knicker H (2004) The effect of fire on soil organic matter - a review. *Environ Int* 30:855–870. <https://doi.org/10.1016/j.envint.2004.02.003>
- Granged AJP et al (2011) Post-fire evolution of soil properties and vegetation cover in a Mediterranean heathland after experimental burning: A 3-year study. *Geoderma* 164(1–2):85–94
- Guadagno FM, Forte R, Revellino P et al (2005) Some aspects of the initiation of debris avalanches in the Campania Region: the role of morphological slope discontinuities and the development of failure. *Geomorphology* 66:237–254. <https://doi.org/10.1016/j.geomorph.2004.09.024>
- Guadagno FM, Revellino P (2005) Debris avalanches and debris flows of the Campania Region (southern Italy). *Debris-flow hazards and related phenomena*. Springer, pp 489–518
- Horton RE (1932) The role of infiltration in the hydrology cycle. *Trans Am Geophys Union* 14:446–460
- Hungre O, Evans SG, Bovis MJ, Hutchinson JN (2001) A review of the classification of landslides of the flow type. *Environ Eng Geosci* 7:221–238. <https://doi.org/10.2113/gseengeosci.7.3.221>
- Iovino F (2007) *Analisi dell'uso del suolo e linee operative di gestione forestale sostenibile per mitigare la vulnerabilità del territorio di Pizzo d'Alvano (Campania)*, vol 2. Quaderni del Camilab
- ISO (2004) *Geotechnical investigation and testing—Laboratory testing of soil—Part 11: Determination of permeability by constant and falling head*, International Organization for Standardization, Geneva, Switzerland (accessed on 15/02/2022)
- Jackson M, Roering JJ (2009) Post-fire geomorphic response in steep, forested landscapes: Oregon Coast Range, USA. *Quat Sci Rev* 28:1131–1146. <https://doi.org/10.1016/j.quascirev.2008.05.003>
- Lei M, Cui Y, Ni J et al (2022) Temporal evolution of the hydromechanical properties of soil-root systems in a forest fire in China. *Sci Total Environ* 809:151165. <https://doi.org/10.1016/j.scitotenv.2021.151165>
- Leung AK, Garg A, Ng CWW (2015) Effects of plant roots on soil-water retention and induced suction in vegetated soil. *Eng Geol* 193:183–197. <https://doi.org/10.1016/j.enggeo.2015.04.017>
- Li XS (2005) Modelling of hysteresis response for arbitrary wetting/drying paths. *Comput Geotech* 32:133–137
- Löbmann MT, Geitner C, Wellstein C, Zerbe S (2020) The influence of herbaceous vegetation on slope stability – a review. *Earth Sci Rev* 209:103328. <https://doi.org/10.1016/j.earscirev.2020.103328>

- Lu N, Likos WJ (2004) Unsaturated soil mechanics. Wiley, Hoboken
- Mallik AU, Gimingham CH, Rahman AA (1984) Ecological effects of heather burning: I. Water Infiltration, Moisture Retention and Porosity of Surface Soil. *J Ecol* 72:767. <https://doi.org/10.2307/2259530>
- Mataix-Solera J, Cerdà A, Arcenegui V et al (2011) Fire effects on soil aggregation: a review. *Earth Sci Rev* 109:44–60. <https://doi.org/10.1016/j.earscirev.2011.08.002>
- McGuire LA, Youberg AM, Rengers FK et al (2021) Extreme precipitation across adjacent burned and unburned watersheds reveals impacts of low severity wildfire on debris-flow processes. *J Geophys Res Earth Surf* 126:e2020JF005997. <https://doi.org/10.1029/2020JF005997>
- Migale LS, Milone A (1998) Colate rapide di fango in terreni piroclastici della Campania. Primi dati della ricerca storica. *Rassegna Storica Salernitana* 15:253–271
- Moody JA, Dungan Smith J, Ragan BW (2005) Critical shear stress for erosion of cohesive soils subjected to temperatures typical of wildfires. *J Geophys Res Earth Surf* 110:1–13. <https://doi.org/10.1029/2004JF000141>
- Moody JA, Shakesby RA, Robichaud PR et al (2013) Current research issues related to post-wildfire runoff and erosion processes. *Earth-Science Rev* 122:10–37. <https://doi.org/10.1016/j.earscirev.2013.03.004>
- Movsat M, Tomac I (2021) Assessment of physical properties of water-repellent soils. *J Geotech Geoenviron Eng* 147:06021010. [https://doi.org/10.1061/\(asce\)gt.1943-5606.0002604](https://doi.org/10.1061/(asce)gt.1943-5606.0002604)
- Mualem Y (1976a) A new model for predicting the hydraulic conductivity of unsaturated porous media. *Water Resour Res* 12:513–522
- Mualem Y (1976b) Hysteretical models for prediction of the hydraulic conductivity of unsaturated porous media. *Water Resour Res* 12:1248–1254
- Nakane K, Nakagawa K, Takahashi F (1983) Change in tensile strength of Japanese red pine roots after death by fire. *J Jpn for Soc* 65:155–165
- Neary DG, Klopatek CC, DeBano LF, Ffolliott PF (1999) Fire effects on belowground sustainability: a review and synthesis. *For Ecol Manage* 122:51–71. [https://doi.org/10.1016/S0378-1127\(99\)00032-8](https://doi.org/10.1016/S0378-1127(99)00032-8)
- Nyman P, Sheridan GJ, Smith HG, Lane PN (2014) Modeling the effects of surface storage, macropore flow and water repellency on infiltration after wildfire. *J Hydrol* 513:301–313
- Olivares L, Damiano E, Netti N, de Cristofaro M (2018) Geotechnical properties of two pyroclastic deposits involved in catastrophic flowslides for implementation in early warning systems. *Geosciences* 9:24. <https://doi.org/10.3390/geosciences9010024>
- Parsons A, Robichaud PR, Lewis SA et al (2010) Field guide for mapping post-fire soil burn severity. USDA Forest Service, US, pp 1–49. <https://doi.org/10.2737/RMRS-GTR-243> (Gen Tech Rep RMRS-GTR)
- Peduto D, Iervolino L, Foresta V (2022) Experimental analysis of the fire-induced effects on the physical, mechanical, and hydraulic properties of sloping pyroclastic soils. *Geosciences* 12:198. <https://doi.org/10.3390/geosciences12050198>
- Picarelli L, Olivares L, Damiano E et al (2020) The effects of extreme precipitations on landslide hazard in the pyroclastic deposits of Campania Region: a review. *Landslides* 17:2343–2358. <https://doi.org/10.1007/s10346-020-01423-5>
- Picarelli L, Vinale F (2007) Messa a punto di modelli geotecnici per la simulazione degli effetti al suolo delle precipitazioni. AMRA (Report-Centro Euro-Mediterraneo per i cambiamenti climatici)
- Pierson TC, Costa JE, Vancouver W (1987) A rheologic classification of subaerial sediment-water flows. *Debris Flows/Avalanches: Process, Recognition, and Mitigation*, vol 7. Geological Society of America, pp 1–12 (Reviews in Engineering Geology)
- Pirone M, Papa R, Nicotera MV, Urciuoli G (2014) Evaluation of the hydraulic hysteresis of unsaturated pyroclastic soils by in situ measurements. *Proced Earth Plan Sci* 9:163–170
- Regelbrugge JC, Conard SG (1993) Modeling tree mortality following wildfire in pinus ponderosa forests in the central sierra nevada of california. *Int J Wildl Fire* 3:139–148. <https://doi.org/10.1071/WF9930139>
- Rengers FK, McGuire LA, Oakley NS et al (2020) Landslides after wildfire: initiation, magnitude, and mobility. *Landslides* 17:2631–2641. <https://doi.org/10.1007/s10346-020-01506-3>
- Rengers FK, McGuire LA, Kean JW, Staley DM, Hobley DEJ (2016) Model simulations of flood and debris flow timing in steep catchments after wildfire. *J Am Water Resour Assoc* 52:6041–6061. <https://doi.org/10.1002/2015WR018176>
- Rianna G, Comegna L, Pagano L, Picarelli L, Reder A (2019) The role of hydraulic hysteresis on the hydrological response of pyroclastic silty covers. *Water* 11(3):628. <https://doi.org/10.3390/w11030628>
- Richards LA (1931) Capillary conduction of liquids through porous mediums. *J Appl Phys* 1:318–333. <https://doi.org/10.1063/1.1745010>
- Robichaud PR (2000) Fire effects on infiltration rates after prescribed fire in northern Rocky Mountain forests, USA. *J Hydrol* 231–232:220–229. [https://doi.org/10.1016/S0022-1694\(00\)00196-7](https://doi.org/10.1016/S0022-1694(00)00196-7)
- Rolandi G, Petrosino P, Mc Geehin J (1998) The interplinian activity at Somma-Vesuvius in the last 3500 years. *J Volcanol Geoth Res* 82:19–52. [https://doi.org/10.1016/S0377-0273\(97\)00056-5](https://doi.org/10.1016/S0377-0273(97)00056-5)
- Schuurman JJ, Goedewaagen MAJ (1971) Methods for the examination of root systems and roots. Vlaardingen
- Shakesby RA, Doerr SH (2006) Wildfire as a hydrological and geomorphological agent. *Earth Sci Rev* 74:269–307. <https://doi.org/10.1016/j.earscirev.2005.10.006>
- Staley DM, Kean JW, Rengers FK (2020) The recurrence interval of post-fire debris-flow generating rainfall in the southwestern United States. *Geomorphology* 370:107392. <https://doi.org/10.1016/j.geomorph.2020.107392>
- Stoof CR, Wesseling JG, Ritsema CJ (2010) Effects of fire and ash on soil water retention. *Geoderma* 159:276–285. <https://doi.org/10.1016/j.geoderma.2010.08.002>
- Tami D, Rahardjo H, Leong EC (2004) Effects of hysteresis on steady-state infiltration in unsaturated slopes. *J Geotech Geoenviron Eng* 130:956–966
- Tarantino A (2009) A water retention model for deformable soils. *Géotechnique* 59:751–762
- Terefe T, Mariscal-Sancho I, Peregrina F, Espejo R (2008) Influence of heating on various properties of six Mediterranean soils. A Laboratory Study. *Geoderma* 143:273–280. <https://doi.org/10.1016/j.geoderma.2007.11.018>
- Tiwari B, Ajmera B, Bennett R (2019) Impact of low shearing resistance of ash deposit on post fire rainfall induced debris flow. IPL Symposium. UNESCO, Paris, pp 57–60
- Tsai TL (2010) Influences of soil water characteristic curve on rainfall-induced shallow landslides. *Environ Earth Sci* 64:449–459. <https://doi.org/10.1007/s12665-010-0868-9>
- Ulery AL, Graham RC (1993) Forest fire effects on soil color and texture. *Soil Sci Soc Am J* 57:135–140. <https://doi.org/10.2136/sssaj1993.03615995005700010026x>
- van Genuchten MT (1980) A closed-form equation for predicting the hydraulic conductivity of unsaturated soils. *Soil Sci Soc Am J* 44:892–898. <https://doi.org/10.2136/sssaj1980.03615995004400050002x>
- Wheeler SJ, Sharma RS, Buisson MSR (2003) Coupling of hydraulic hysteresis and stress-strain behaviour in unsaturated soils. *Géotechnique* 53:41–54
- Woods SW, Balfour V (2006) Effect of vegetative ash on infiltration rates after forest wildfire in the Northern Rocky Mountain region, U.S.A. *Biohydrology Conference 2006*, Prague, Czech Republic, 20–22 Sept 2006

- Woods SW, Balfour VN (2008) The effect of ash on runoff and erosion after a severe forest wildfire, Montana, USA. *Int J Wildl Fire* 17:535–548. <https://doi.org/10.1071/WF07040>
- Woods SW, Balfour VN (2010) The effects of soil texture and ash thickness on the post-fire hydrological response from ash-covered soils. *J Hydrol* 3930:274–286
- WRB (2006) World reference base for soil resources 2006. FAO Press, Rome, Italy (Reports, 103)
- Wu TH (2013) Root reinforcement of soil: review of analytical models, test results, and applications to design. *Can Geotech J* 50:259–274. <https://doi.org/10.1139/cgj-2012-0160>
- Yang C, Sheng D, Carter JP (2012) Effect of hydraulic hysteresis on seepage analysis for unsaturated soils. *Comput Geotech* 41:36–56
- Zhu H, Zhang LM (2016) Field investigation of erosion resistance of common grass species for soil bioengineering in Hong Kong. *Acta Geotech* 11(5):1047–1059. <https://doi.org/10.1007/s11440-015-0408-6>